Broadband acoustic shape optimization of studs in double-leaf walls

Jan C.E. Van den Wyngaert[a], Mattias Schevenels[b], Edwin P.B. Reynders[a]

[a]*KU Leuven, Faculty of Engineering Science, Department of Civil Engineering, Kasteelpark Arenberg 40, B-3001 Leuven, Belgium.*
[b]*KU Leuven, Faculty of Engineering Science, Department of Architecture, Kasteelpark Arenberg 1, B-3001 Leuven, Belgium*

Abstract

Design optimization of vibro-acoustic systems over a wide frequency band is challenging. It does not only require a computationally efficient numerical prediction model of sufficient accuracy, but the optimization scheme itself should also be computationally efficient and the design space should be limited by all relevant manufacturing and performance constraints. In this paper, a methodology is presented for the shape optimization of components in a complex wall system, with the aim of achieving an optimized sound insulation of the overall system across the entire building acoustics frequency range. As an example, the cross-sectional shape of studs in a double-leaf wall is first parameterized and subsequently optimized for broadband sound insulation with a gradient-based optimization scheme. A recently developed sound insulation prediction model that has the required balance between accuracy and computational efficiency is adopted and validated for a range of plasterboard walls with acoustic studs. The model is further complemented with a novel sensitivity analysis, such that the sensitivities of the predicted sound insulation to the cross-sectional stud shape parameters can be obtained in a semi-analytic way. This approach reduces the computation cost related to broadband acoustic design optimization significantly. Furthermore, inequality constraints that are necessary for obtaining a feasible design in terms of material usage and manufacturing limitations are identified and incorporated in the optimization procedure. The relevant constraints related to strength and stiffness of the wall are very mild and therefore verified after optimization. As an example of the proposed methodology, the cross-sectional shape of flexible metal studs in double-leaf plasterboard walls is optimized for the overall A-weighted sound reduction under pink noise excitation. A range of combinations in stud depths and number of sheets is analyzed. Walls containing the optimized studs have an airborne sound insulation that is close to that of walls with fully decoupled leafs. Their sound insulation is on average 11.8 dB higher than when they would contain conventional C-shaped studs, and 5.1 dB higher than when they would contain acoustic studs that are presently available.

Keywords:
shape optimization, double-leaf wall systems, sensitivity analysis, manufacturing constraints, airborne sound insulation

1. Introduction

Double-leaf walls are often employed in the construction, aerospace, marine, railway, and other industries since they can achieve a high sound insulation with a relatively low weight. The leafs are usually coupled to a common frame to reduce the total wall thickness and to ensure a sufficient lateral stiffness, even if the wall is not load bearing. However, by coupling the wall leafs to the common metal frame, a structural transmission path between both leafs is created, therefore lowering the sound insulation (at least above mass-spring-mass resonance where the leafs vibrate as rigid masses, compressing the cavity fluid). A typical example is that of a plasterboard wall where the leafs are screwed into a metal stud frame. When plasterboard walls that are constructed with conventional C-shaped studs, with existing acoustic studs (i.e., more flexible studs with a better acoustic performance), and with decoupled leafs are compared with respect to sound insulation performance, the potential of optimizing the cross-sectional shape of the studs becomes clear, as will be demonstrated in the present study (Section 2.3). Shape optimization is widely applied in the automotive industry, e.g., for finding the optimal shape of steel panels with respect to stiffness, structural vibration or radiated sound[1]. However, the numerical design optimization of sound insulation is most often limited to a single frequency or a narrow frequency band when flexible structures are involved [2, 3, 4], while broadband

optimization is performed for structures with a small number of eigenmodes in the frequency band of interest [5, 6].

Acoustic design optimization of complex structures over a wide frequency band remains very challenging for computational reasons. The behavior of double-leaf walls with a flexible frame is complex since the cross-section of the studs is highly deformable, many physical phenomena contribute to the diffuse airborne sound insulation in the acoustic frequency range, and the walls exhibit a large number of structural modes in this frequency range. Until very recently, one of the obstacles for broadband numerical design optimization has been that the quantitative prediction of the airborne sound insulation of these types of walls was either prohibitively inaccurate or computationally expensive. A recently developed sound insulation prediction model that has the required balance between accuracy and computational efficiency [7] has been the first step in opening up the way for acoustic design optimization. However, other issues remain, including the development of a computationally efficient framework for broadband vibro-acoustic design optimization and the incorporation of relevant design constraints in the optimization process.

In the present work, these fundamental issues are resolved such that broadband acoustic design optimization is achieved. A first contribution is that the general hybrid deterministic-statistical energy analysis (Det-SEA) sound insulation prediction framework [8, 9, 10] is complemented with the derivation of the sensitivities of the coupling loss factor and the airborne sound insulation to the system matrices. As a result, these sensitivities can be efficiently evaluated and broadband optimization with a sensitivity-based approach becomes feasible for a wide range of systems.

Next, the optimization methodology is worked out in detail such that the cross-sectional shape of the studs in a double-leaf wall can be optimized for the broadband airborne sound insulation. In shape optimization, the amount of freedom that is allowed by the analyst - i.e., the amount of shape basis functions - may vary from a single parameter to all nodes in the FE model [11]. The stud shape is discretized using a limited number of points where the steel can possibly be folded. The coordinates of these points are taken to be the design variables. To quantify the broadband acoustic performance of the wall in an unambiguous way, the broadband sound insulation is rated with a standardized single-number rating [12], that serves as objective function in the optimization procedure. The sensitivities of the objective function with respect to the design variables are obtained by means of a semi-analytical approach [13]: the sensitivity of the transmission loss with respect to the system matrices is computed analytically, while the sensitivity of the system matrices with respect to the shape parameters is computed on element level by means of the finite difference method. A similar approach has been followed previously in a different context for optimizing the shape of the cellular cores in a sandwich structure for minimum sound radiation [14] yet for a much stiffer structure. To increase the computational efficiency, the resulting sensitivities are rearranged as the product of terms that only depend on the state of the system and the sensitivities of the system matrices, such that the sensitivities of the sound insulation can be obtained in a computationally efficient way. Although the focus in this work is on the shape optimization of a specific single number sound insulation quantity and on studs with a symmetric cross-sectional shape, the proposed methodology can also be applied to other performance indicators and connector parameterizations.

The incorporation of geometric manufacturing constraints into the broadband acoustic shape optimization process is a third contribution. Inequality constraints are placed on the maximal amount of material used and on the minimal rolling angle between the web elements during optimization to ensure the manufacturability of the metal studs. The relevant constraints related to strength and stiffness of the wall are very mild and therefore verified after optimization.

Subsequently, a range of walls, comprising different combinations in stud depths and number of sheets, are optimized using the proposed framework. The performance of each wall with optimized studs is compared against walls with conventional C-shaped studs and acoustic studs that are presently available. It is found that the optimized walls have a substantially higher broadband sound insulation, close to that of walls with fully decoupled leafs.

The sound insulation prediction model that is employed in the optimization procedure has been validated on a wide range of plasterboard wall systems with conventional C-shaped studs [7]. In the present paper, additional validations on walls with acoustic studs are presented. They confirm the accuracy of the prediction model also for walls with very flexible studs and therefore provide confidence in the validity of the optimization results.

The remainder of this paper is structured as follows. A concise overview of the prediction model for the airborne sound insulation of finite sized double-leaf walls with a flexible frame is provided in section 2. This section also contains a validation of the prediction model for a range of walls with existing acoustic studs as well as a demonstration of the further optimization potential. In section 3, the optimization problem is stated and the manufacturing constraints and the sensitivity of the diffuse sound insulation are elaborated. The results of the optimization are discussed in section 4 and a physical interpretation is provided in section 5. The conclusions and final remarks are listed in section 6. The derivation of the sensitivities of the coupling loss factor is elaborated in the appendix.

2. Sound insulation of double-leaf walls with a common stud frame

2.1. Diffuse sound insulation prediction

The diffuse sound insulation of finite sized, double-leaf walls coupled to a common frame is predicted using the model that was proposed in [7]. The wall is modeled deterministically to capture its vibration behavior in full detail. The sound field in the sending is taken to be diffuse such that the diffuse sound insulation of the wall is obtained. The fundamentals of the diffuse sound transmission model are briefly recalled in the following Sections. For a detailed elaboration of the equations, the reader is referred to [7].

2.1.1. Wall model

The considered wall consists of two leafs separated by an air cavity and coupled with a common stud frame. In the first instance, the leafs, the cavity and the individual studs are decoupled from each other. The assumed-modes method [15] is then used for approximating the vibration field of the two wall leafs, u_{l1} and u_{l2}, the sound pressure field within the cavity, p_{cav}, and the vibration field of the stud number l, $u_{st,l}$, at spatial location $\mathbf{x}$ and frequency ω, using a finite set of basis functions ϕ, that satisfy the boundary conditions. Subsequently, the interaction between the components is achieved by introducing coupling loads between the cavity and the leafs and by constraining the leaf and stud displacements to be equal at the connection locations. This results in a system of equations that couples the generalized degrees of freedom (DOFs) of the wall components. Since the external loading on the wall by the sound pressure in the adjoining rooms is only applied at the leafs, the equations of motion of the wall can be elaborated in terms of the interface DOFs, $\mathbf{q}_{\ell 1}$ and $\mathbf{q}_{\ell 2}$ of respectively wall leaf 1 and 2, as follows

$$\mathbf{D}'_{\mathrm{d}}\mathbf{q}' = \mathbf{f}', \tag{1}$$

where $\mathbf{D}'_{\mathrm{d}}$ is the dynamic stiffness matrix of the wall in terms of the interface DOFs $\mathbf{q}' = \begin{bmatrix} \mathbf{q}_{\ell 1}^{\mathrm{T}} & \mathbf{q}_{\ell 2}^{\mathrm{T}} \end{bmatrix}^{\mathrm{T}}$ and $\mathbf{f}'$ are the forces on these DOFs due to the sound pressure field in the adjoining rooms. The dynamic stiffness matrix in Eq. (1) can be split up into three terms: the contribution of the decoupled wall leafs, the contribution of the cavity through the Fluid-Structure Interaction (FSI) with the wall leafs, and the contribution of the studs through structural coupling to the wall leafs:

$$\mathbf{D}'_{\mathrm{d}} = \begin{bmatrix} \mathbf{D}_{\ell 1} & \mathbf{0} \\ \mathbf{0} & \mathbf{D}_{\ell 2} \end{bmatrix} + \mathbf{D}'_{\mathrm{fsi}} + \mathbf{D}'_{\mathrm{st}}, \tag{2}$$

with $\mathbf{D}_{\ell 1}$ and $\mathbf{D}_{\ell 2}$ the dynamic stiffness matrices of respectively wall leaf 1 and 2, $\mathbf{D}'_{\mathrm{fsi}}$ the fluid-structure interaction matrix that takes into account the acoustic coupling between the wall leafs through the cavity and $\mathbf{D}'_{\mathrm{st}}$ the matrix that takes into account the structural coupling between the wall leafs through the common metal stud frame.

The thin plates can be fairly accurately modeled as simply supported Kirchoff-Love plates [16]. The leaf may consist of a single thin plate, or of multiple plates on top of each other. In the latter case, it is reasonable to assume that there are no shear connections between the plates, such that perfect slip conditions exist at the plate-plate interfaces [17]. At frequency ω, the elements of the diagonal matrix $\mathbf{D}_{\ell j}$ read

$$\mathrm{D}_{\ell j,kk} = -\omega^2 + \omega_{\ell j,k}^2(1+\mathrm{i}\eta_{\ell j,k}), \qquad \omega_{\ell j,k} = \sqrt{\frac{\mathrm{D}_{\ell j}}{\mathrm{m}''_{\ell j}}\left(\left(\frac{q_k\pi}{\mathrm{L_x}}\right)^2 + \left(\frac{r_k\pi}{\mathrm{L_y}}\right)^2\right)}, \qquad \mathrm{D}_{\ell j} = \sum_{n=1}^{\mathrm{n_{pl,j}}} \frac{\mathrm{E}_{n,j}\mathrm{t}_{n,j}^3}{12(1-\nu_{n,j}^2)}, \tag{3}$$

where $\mathrm{i} = \sqrt{-1}$ is the imaginary unit, $\mathrm{m}''_{\ell j}$ denotes the surface mass of leaf j, $\mathrm{n_{pl,j}}$ are the number of plates in leaf j, $\mathrm{L_x}$ and $\mathrm{L_y}$ denote its planar dimensions in the x and y coordinate directions, respectively, $q_k, r_k \in \mathbb{N}_0$ denote the number of half wavelengths in those directions and $\eta_{\ell i,k}$ denotes the damping loss factor of mode k. $\mathrm{E}_{n,j}$ is the Young's modulus of plate n in leaf j, $\nu_{n,j}$ its Poisson's ratio, and $\mathrm{t}_{n,j}$ its thickness.

The sound field in the cavity satisfies the homogeneous Helmholtz equation. The interaction between the sound field in the cavity and the studs is neglected, i.e., the studs are assumed to be acoustically transparent, such that the cavity has a rectangular cuboid shape. The walls that are considered in this paper contain mineral wool inside the cavity. The Delany-Bazley-Miki equivalent fluid model [18] is used to model this soft porous material. The interaction

between the wall leafs and the cavity accounted for by considering the loading by the displacement fields of the wall leafs onto the cavity pressure field and vice versa:

$$\mathbf{D}'_{\mathrm{fsi}} = -\rho_{\mathrm{a}}\omega^2 \begin{bmatrix} \mathbf{L}_{\mathrm{f1}} \\ \mathbf{L}_{\mathrm{f2}} \end{bmatrix} \mathbf{D}_{\mathrm{cav}}^{-1} \begin{bmatrix} \mathbf{L}_{\mathrm{f1}}^{\mathrm{T}} & \mathbf{L}_{\mathrm{f2}}^{\mathrm{T}} \end{bmatrix}, \tag{4}$$

where $\mathbf{D}_{\mathrm{cav}}$ is the diagonal dynamic stiffness matrix of the cavity in therms of its hard-walled modal DOFs

$$\mathrm{D}_{\mathrm{cav},kk} = -\omega^2 + \omega_{\mathrm{cav},k}^2(1 + \mathrm{i}\eta_{\mathrm{cav},k}), \qquad \omega_{\mathrm{cav},k} = \mathrm{c}\sqrt{\left(\frac{m_k\pi}{\mathrm{L}_{\mathrm{x}}}\right)^2 + \left(\frac{n_k\pi}{\mathrm{L}_{\mathrm{y}}}\right)^2 + \left(\frac{p_k\pi}{\mathrm{t}_{\mathrm{cav}}}\right)^2}, \tag{5}$$

m_k, n_k, $p_k \in \mathbb{N}$ denote the number of half wavelengths in the x, y and z coordinate directions, $z_1 = 0$, $z_2 = \mathrm{t}_{\mathrm{cav}}$, c denotes the speed of sound in air, ρ_{a} is the density of air, $\mathrm{t}_{\mathrm{cav}}$ is the cavity depth and $\mathrm{t}_{\mathrm{tot}}$ is the total leaf thickness. $\mathrm{L}_{\mathrm{f}i,kl}$ is the fluid structure interaction matrix between the k-th DOF of wall leaf i and the j-th DOF of the cavity

$$\mathrm{L}_{\mathrm{f}i,kl} = \frac{-2a_l\mathrm{L}_{\mathrm{x}}\mathrm{L}_{\mathrm{y}}}{\pi^2\sqrt{\mathrm{t}_{\mathrm{tot}}m_{\ell i}''}} \cos\left(\frac{p\pi z_i}{\mathrm{t}_{\mathrm{cav}}}\right) \mathrm{b}\left(q_k, m_l\right) \mathrm{b}\left(r_k, n_l\right), \tag{6}$$

$$a_l = \frac{\mathrm{c}\gamma(m_l)\gamma(n_l)\gamma(p_l)}{\sqrt{\mathrm{L}_{\mathrm{x}}\mathrm{L}_{\mathrm{y}}\mathrm{t}_{\mathrm{cav}}}}, \quad \gamma(s) = \begin{cases} \sqrt{2} & \text{if } s = 0 \\ 1 & \text{if } s \neq 0 \end{cases}, \quad \mathrm{b}\left(\alpha, \beta\right) = \begin{cases} \frac{\beta\cos(\alpha\pi)\cos(\beta\pi)-\beta+\alpha\sin(\alpha\pi)\sin(\beta\pi)}{\alpha^2-\beta^2} & \text{for } \alpha \neq \beta \\ 0 & \text{for } \alpha = \beta \end{cases}. \tag{7}$$

The studs are modeled numerically, using the finite element method [19], with structural shell elements. Pinned boundary conditions are assumed at the ends of each stud; they are implemented by restraining all nodal displacements (but not the rotations) at one flange at the bottom and at the opposite flange at the top. The stud-leaf connections are modeled by rigidly coupling the out of plane displacements at the screw locations. Since thin metal studs themselves are a lot more flexible than the plate-stud connections by the screws, the assumption of rigid connections is accurate. The structural coupling is taken into account by constraining the displacements of the wall leafs and the studs to be equal at the screw locations. As a result the matrix $\mathbf{D}'_{\mathrm{st}}$ which appears in (2) is comprised of the dynamic stiffness matrix $\mathbf{D}_{\mathrm{st}}$ of the stud in terms if its generalized, decoupled modal DOFs, and a series of coupling matrices:

$$\mathbf{D}'_{\mathrm{st}} = \begin{bmatrix} \mathbf{C}_{\ell 1}^T \\ \mathbf{C}_{\ell 2}^T \end{bmatrix} \left(\sum_{k=1}^{\mathrm{n}_{\mathrm{st}}} \mathbf{C}_k \mathbf{D}_{\mathrm{st}}^{-1} \mathbf{C}_k^T\right) \begin{bmatrix} \mathbf{C}_{\ell 1} & \mathbf{C}_{\ell 2} \end{bmatrix}, \tag{8}$$

$$\mathrm{D}_{\mathrm{st},kk} = -\omega^2 + \omega_{\mathrm{st},k}^2(1 + \mathrm{i}\eta_{\mathrm{st},k}), \tag{9}$$

where $\mathbf{C}_{\ell 1}$ and $\mathbf{C}_{\ell 2}$ are coupling matrices for wall leafs 1 and 2, $\mathbf{C}_k$ is a coupling matrix for stud k and n_{st} denotes the total number of studs in the double-leaf wall. The precise definition of the coupling matrices can be found in [7].

2.1.2. Sound transmission model

Within the hybrid Det-SEA framework [8, 20, 21], a transmission suite (room-wall-room) model has been developed for predicting the diffuse sound transmission loss of finite-sized walls of arbitrary complexity [9, 22, 10]. The sending and receiving room are modeled as diffuse (SEA) subsystems, while the detailed model of the wall is deterministic. In the context of a sound transmission analysis, the quantity of interest is the so-called coupling loss factor, η_{12}, between both rooms. This coupling loss factor relates directly to the diffuse sound transmission coefficient τ. The relationship at frequency ω reads [23]

$$\tau = \frac{4V_1\omega}{\mathrm{L}_{\mathrm{x}}\mathrm{L}_{\mathrm{y}}c}\eta_{12}, \tag{10}$$

where V_1 denotes the volume of the sending room. The sound insulation of the wall then immediately follows from

$$\mathrm{R}(\omega) = 10\log\frac{1}{\tau} = 10\log\frac{\mathrm{L}_{\mathrm{x}}\mathrm{L}_{\mathrm{y}}c}{4V_1\omega\eta_{12}}. \tag{11}$$
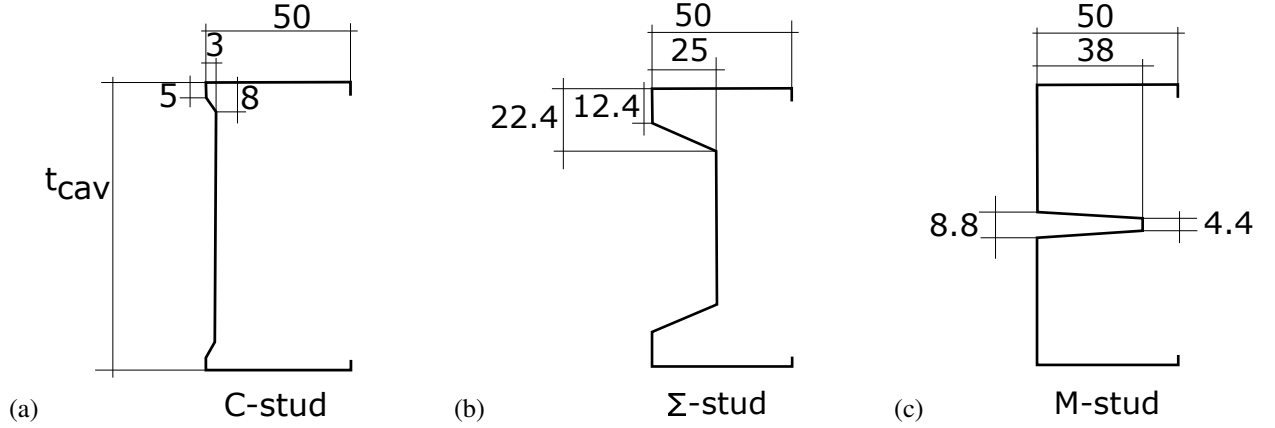
4

Figure 1: Dimensions of the cross sectional shape of (a) a C-shaped stud, (b) a Σ-shaped stud and (c) an M-shaped stud, all dimensions are given in mm.

With the hybrid Det-SEA framework, the coupling loss factor can be rigorously obtained from [8]

$$\eta_{12} = \frac{2}{\pi \omega n_1} \sum_{r,s} \mathrm{Im} \left(\mathbf{D}'_{\mathrm{dir2}}\right)_{rs} \left(\mathbf{D}_{\mathrm{tot}}^{-1} \mathrm{Im} \left(\mathbf{D}'_{\mathrm{dir1}}\right) \mathbf{D}_{\mathrm{tot}}^{-H}\right)_{rs}, \tag{12}$$

where

$$\mathbf{D}_{\mathrm{tot}} = \mathbf{D}'_{\mathrm{d}} + \mathbf{D}'_{\mathrm{dir1}} + \mathbf{D}'_{\mathrm{dir2}}. \tag{13}$$

$\mathbf{D}'_{\mathrm{d}}$ denotes the reduced dynamic stiffness matrix of the wall as defined in Eq. (1), $\mathbf{D}'_{\mathrm{dir1}}$ and $\mathbf{D}'_{\mathrm{dir2}}$ are the direct field acoustic dynamic stiffness matrices of the rooms expressed in terms of the generalized wall DOFs related to $\mathbf{q}'$ and n_1 is the modal density in the first transmission room. The direct field response of a room is the sound field that would occur if the room would be of infinite extent, in other words, if the room would behave as an acoustic half-space as seen from the room-wall interface when that interface is embedded in an infinite planar baffle. The related acoustic dynamic stiffness matrix is then termed the direct field dynamic stiffness matrix $\mathbf{D}_{\mathrm{dir}}$ of the room. For room 1 for example, the direct field dynamic stiffness matrix $\mathbf{D}_{\mathrm{dir1}}$ describes the relationship between the displacements and forces at the interface with the first wall leaf

$$\mathbf{D}_{\mathrm{dir1}} \mathbf{u}_{\ell 1} = \mathbf{f}_{\mathrm{dir1}}, \tag{14}$$

where the components of $\mathbf{f}_{\mathrm{dir1}}$ denote the forces acting on the DOFs of the first wall leaf $\mathbf{u}_{\ell 1}$ due to the pressure field in the acoustic half-space. In the present work, $\mathbf{D}_{\mathrm{dir1}}$ and $\mathbf{D}_{\mathrm{dir2}}$ are computed using a wavelet approach [24]. In this way, the cross-modal coupling of the wall modes by the acoustic fluid is accounted for [10].

2.2. Validation of the prediction model for walls with acoustic studs

The diffuse sound insulation prediction model has been validated on a range of plasterboard walls with conventional C-shaped studs [7]. In the present work, the prediction model is employed for the analysis and optimization of walls with very flexible, acoustic studs. Therefore, an additional validation is presented here for a set of nine different plasterboard walls with acoustic studs that have been tested in the transmission suite of the KU Leuven Acoustics Laboratory.

The transmission opening has a width of 3.25 m and a height of 2.95 m. All walls contain seven studs in total, two of which are placed against the vertical edges of the opening, and five in between. The center to center distance between two adjoining studs equals 400 mm at the left and right hand side of the test opening and 600 mm in between. In order to connect a plasterboard plate to a metal stud, twelve screws are used along the vertical plate edge. Screws start at 100 mm from the bottom edge and end at 100 mm from the top edge of a plate. The vertical distance between two screws is 250 mm. The studs are either Σ-shaped (Fig. 1.b) or M-shaped (Fig. 1.c). They have a thickness of

0.6 mm. Plasterboard plates with a density of $1008\,\mathrm{kg/m^3}$ and a Young's modulus of 3.15 GPa have been used in conjunction with the Σ-shaped studs, while for the walls with M-shaped studs, the values are $1060\,\mathrm{kg/m^3}$ and 5.4 GPa, respectively. The densities have been determined by weighing, and the Young's moduli by modal testing on small plate samples [25, 26]. The leafs of each wall can consist of one, two or three plasterboard sheets of $12.5\,\mathrm{mm}$ thickness each. The cavity depth is either 50, 75 or $100\,\mathrm{mm}$. The cavity is filled with mineral wool. Each of the tested wall is labeled by the combination of the number of sheets constituting one leaf, the thickness of a single sheet in mm, the cavity depth in mm, the cavity filling, and the stud type. For example, the wall labeled as 2x12.5/75 mw (Σ) has leafs with double plasterboard sheet at each side, an individual sheet thickness of 12.5 mm, a cavity with a depth of 75 mm and mineral wool filling, and Σ-shaped studs.

In the simulations, the assumed material properties for the galvanized steel studs are: a Young's modulus of 210 GPa, a density of 7800 kg/m^3, a Poisson's ratio of 0.25, a damping loss factor of 0.02 and a yield strength of 210 MPa. The damping loss factor of the plates is taken to be 0.03, as in [7]. Their Poisson's is chosen to match the experimental coincidence frequency in one of the sound transmission tests. This results in a Poisson's ratio of 0.15 and 0.10 for the plates that are used in conjunction with the Σ-shaped and M-shaped studs, respectively. The density and sound speed of air are taken as 1.21 kg/m^3 and 340 m/s, respectively. The flow resistivity of the mineral wool, used as sound absorbent in the cavity, is estimated at 5000 N/sm^4 [7].

The measured and predicted transmission loss curves as a function of frequency are displayed in Fig. 2. The single number ratings according to ISO 717 - 1 [12] are listed in Table 1. A good agreement between the model predictions and the experimental results can be observed. The ISO 12999-1 standard [27] defines an average experimental reproducibility for the single number ratings R_w, $R_\mathrm{w} + C$ and $R_\mathrm{w} + C_\mathrm{tr}$ as respectively 2.0, 2.1 and 2.4 dB for a 95 % confidence interval. From Table 1, it can be concluded that for nearly all walls, the predicted single-number ratings differ from the experimental values by 0 to 2 dB which is close to the average reproducibility with a coverage probability of 95 % for experiments.

Wall type	$R_\mathrm{W}(C; C_\mathrm{tr})_\mathrm{exp}$ dB	$R_\mathrm{W}(C; C_\mathrm{tr})_\mathrm{model}$ dB
1x12.5/50 mw (Σ)	45(-5;-13)	43(-4;-11)
2x12.5/50 mw (Σ)	58(-6;-13)	56(-5;-14)
3x12.5/50 mw (Σ)	62(-3;-9)	62(-4;-11)
1x12.5/75 mw (Σ)	50(-6;-14)	48(-7;-16)
2x12.5/75 mw (Σ)	61(-4;-11)	60(-4;-12)
3x12.5/75 mw (Σ)	65(-2;-7)	66(-4;-10)
1x12.5/75 mw (M)	49(-4;-11)	49(-5;-13)
2x12.5/75 mw (M)	60(-3;-10)	61(-3;-8))
2x12.5/100 mw (M)	61(-3;-8)	61(-2;-6)

Table 1: Comparison of the experimental results and predictions of the single number ratings for 9 double leaf plasterboard walls with acoustic studs.

2.3. Optimization potential

To illustrate the optimization potential of the cross-sectional shape of the studs, the airborne sound insulation is computed according to Eq. (11) for a double-leaf plasterboard wall with double sheet and a cavity of 75 mm filled with mineral wool. Each sheet has a thickness of 12.5 mm. A wall with decoupled leafs is compared to walls with a common frame that consists of either C-shaped studs, Σ-shaped studs or M-shaped studs. The cross-sectional shapes of these studs are given in Fig. 1. The geometrical parameters of the wall and the material properties of the studs are the same as in Section 2.2. All walls have conventional plasterboard plates, with a density of 720 kg/m^3, a Young's modulus of 2.5 GPa, a Poisson's ratio of 0.3 and a damping loss factor of 0.03 [7]. As a result, the considered walls only differ in terms of the cross-sectional shape of the studs.

The computed sound insulation curves are displayed in Fig. 3. At around $63\,\mathrm{Hz}$, a dip is observed for the walls with a the most flexible, Σ-shaped and M-shaped studs and for the wall with decoupled leafs. The dip is caused by the
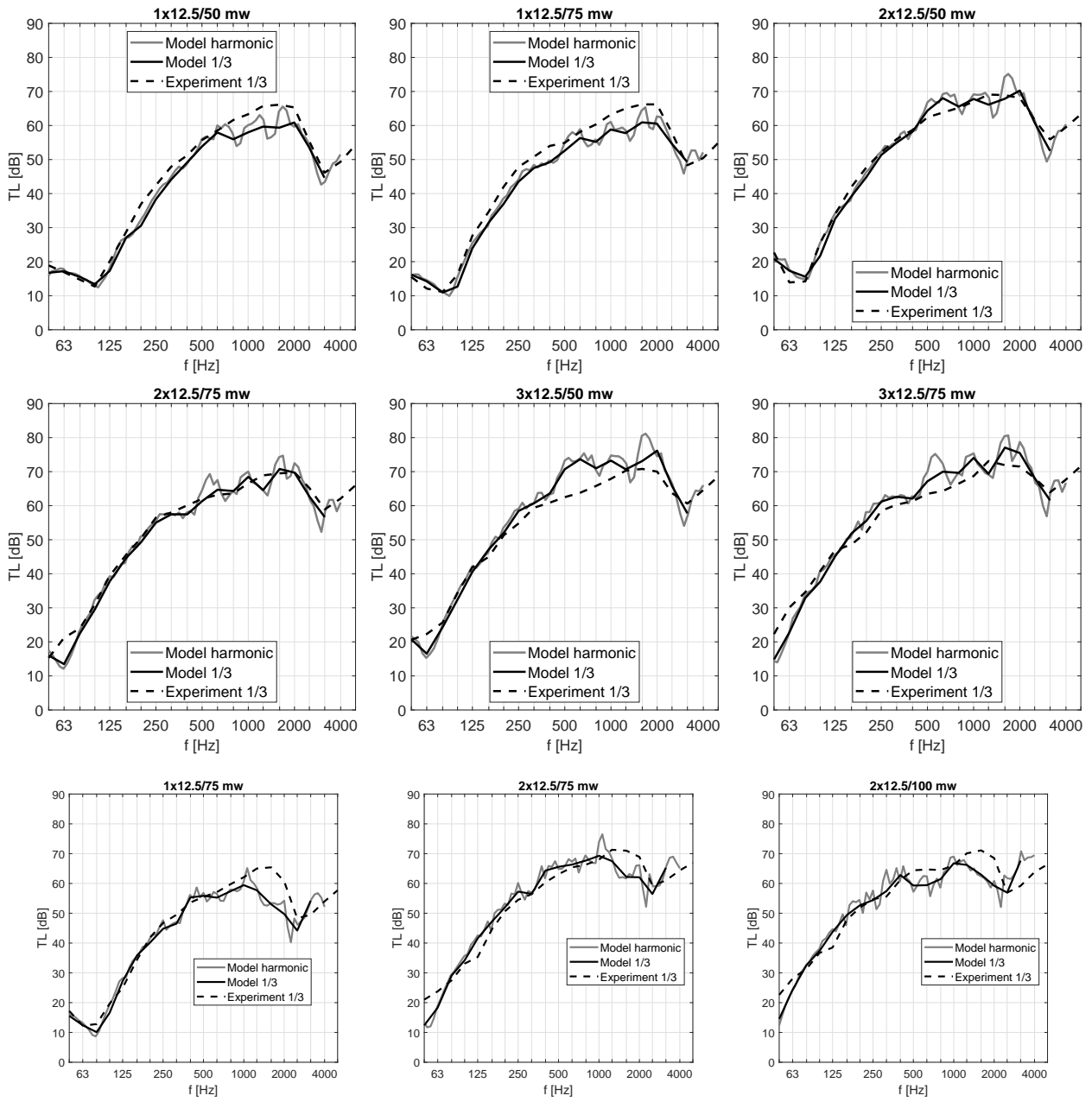
Figure 2: Predicted versus measured airborne sound insulation for nine double leaf plasterboard walls with acoustic studs.

so called mass-spring-mass resonance for double leaf walls. For an infinite double wall without studs, the leafs vibrate as rigid masses and compress the cavity fluid. For a finite studded wall, the mass-spring-mass resonance cannot fully develop due to restrained motion at the leaf edges and the presence of the studs, but the resulting sound insulation dip is nevertheless observed. The least flexible, C-shaped studs, attenuate the mass-spring-mass resonance better and therefore the sound insulation is higher for the corresponding wall around the resonance frequency. Above the mass-spring-mass resonance though, the wall constructed with the C-shaped studs has a significantly lower airborne sound insulation compared to the more flexible studs and the decoupled wall, due to the substantially higher structural coupling of the wall leafs.

At high frequencies, a pronounced dip appears in all sound insulation curves (Fig. 3). This is the so-called coincidence dip. It occurs at the critical frequency of a single plasterboard sheet, i.e., the lowest frequency at which the free bending wavelength on an infinite leaf matches the projected free wavelength in air. The theoretical value of the critical frequency is 2728 Hz for the plates considered here. The coincidence frequency does not change significantly when a different stud type is employed.

When comparing the airborne sound insulation of the decoupled wall and the C-shaped studded wall, a difference of up to 21 dB is observed for the 1/3-octave bands above the mass-spring-mass resonance. The difference in single number rating R_A is 11.6 dB. When comparing the airborne sound insulation of the wall with the decoupled leafs and the wall constructed with a Σ-shaped stud frame, i.e. an experimentally optimized stud, a difference up to 16 dB is observed for the 1/3-octave bands above the mass-spring-mass resonance. The difference in the broadband single number rating $R_w + C$ is 4.5 dB. This illustrates the potential for further numerical design optimization.
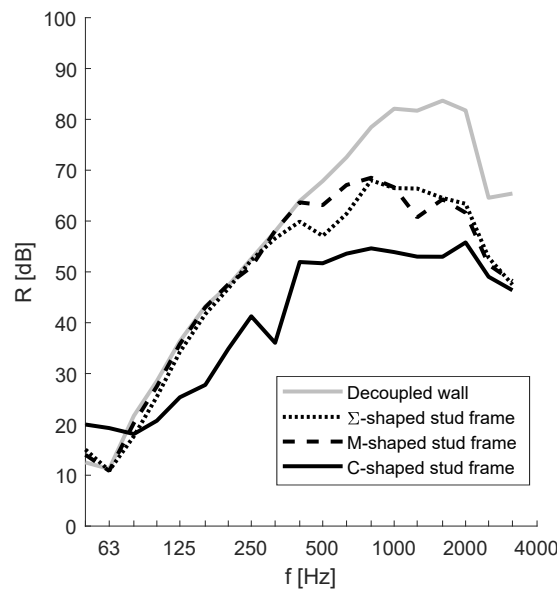

Figure 3: A comparison of the airborne sound insulation of a double plasterboard wall with decoupled leafs and walls constructed with a Σ-shaped stud frame, an M-shaped stud frame and a C-shaped stud frame.

3. Optimization methodology

In this section, a methodology for optimizing the design of wall and floor systems for broadband airborne sound insulation is developed. The methodology is illustrated in detail for the optimization of the cross-sectional shape of metal studs in a double-leaf wall. It can be readily extended to other shape optimization cases.

3.1. Wall setup

The material and geometrical properties of the walls used in the optimization are the same as in Sec. 2.2. Walls with a cavity depth of 50, 75, 100 and 150 mm, and with single, double and triple sheet are considered.

3.2. Parametrization

The cross-sectional shape of the metal studs is described by the design variables that are to be optimized. To avoid infeasible shapes, piece-wise polynomial functions are often employed to describe a shape [28]. Metal studs in plasterboard walls usually have an open cross-section consisting of a small number of straight line segments and sometimes also a few curved segments. A piecewise linear shape is therefore considered here. This parametrization scheme greatly reduces the number of design variables as in practice the number of line segments is often kept to a minimum for reasons of production cost [29]. However, this parametrization could still lead to unfeasible, jagged solutions. Therefore, geometric constraints are needed to reduce the risk of finding these unwanted designs.

The x-coordinates of the keypoints that define the piecewise linear shape (see Fig. 4), are used as design variables. They are collected in the vector $\mathbf{x}$. At half the depth of the cross-section of the stud, a symmetry plane is assumed. The number of unknowns in the numerical design optimization is effectively halved in this way. The optimization is performed for N = 7 keypoints. To prevent that screws, which typically have a length of 25 mm, can penetrate the web of the stud when the wall is constructed, a minimal distance of 12.5 mm is kept between the protruding parts of the web and the flanges of the stud. The keypoints are evenly spaced in the y-direction in the interval $[12.5 \, \mathrm{mm}, t_{\mathrm{cav}}/2 - \mathrm{d}]$ with t_{cav} the depth of the cavity. The x-coordinates have lower and upper bounds of respectively 0 mm and W = 50 mm. This ensures that no web member lies outside the bounds defined by the flanges of the stud. An example of the parametrization of the cross-sectional shape of a metal stud is displayed in Fig. 4.

Although the focus in this paper is on the shape optimization of studs with a symmetric cross section, the proposed methodology can also be applied to other connectors, such as asymmetric or point-symmetric studs.
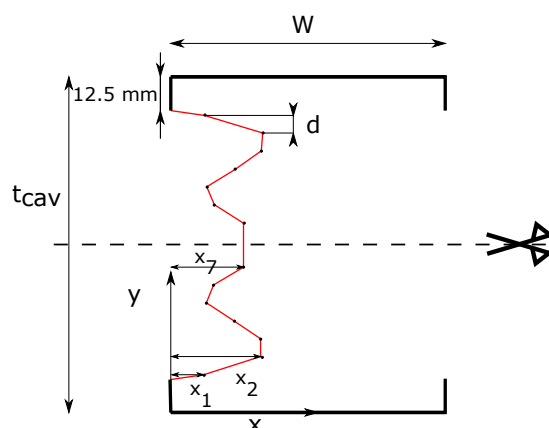

Figure 4: Example of a parametrization of a symmetric stud. In this example 7 design variables are used with the keypoints spaced evenly by a distance d in the y-direction. The stud has a width of W and a web height of t_{cav}. An axis of symmetry is assumed at half the stud depth.

3.3. Objective function

The sound insulation of a wall is a property that depends on the frequency, the wall setup and the rooms adjacent to the wall, as shown in Eqs. (11)-(12). To quantify the broadband acoustic performance of the wall in an unambiguous way, the sound insulation is reduced to a single number. For partitioning walls, the single number rating $R_W + C$ is often used and is therefore taken as the objective function. This single number rating uses a correction which best represents the performance of indoor walls. In the remainder of this paper, the single number rating $R_W + C$ will be denoted as R_A. The single number rating R_A relates directly to the A-weighted sound pressure level difference across a partition wall when the excitation signal in the sending room is pink noise in the frequency bands of 100-3150 Hz and the absorption in the receiving room is the same in all frequency bands. It is defined as [12]:

$$R_A = -10 \log \left(\sum_{j=1}^{16} 10^{(L_{1j} - X_j)/10} \right), \tag{15}$$

where X_j is the mean airborne sound insulation in the j-th 1/3 octave band and L_{1j} is the corresponding spectral adaptation term. The values of L_{1j} are listed in ISO 717-1 [12]. The airborne sound insulation in any 1/3 octave band j is obtained as the energetic mean of the computed harmonic sound insulation values at frequencies ω_j in band Ω_j. This results in the following expression for the averaged sound insulation in 1/3 octave bands in the frequency band j:

$$X_j = -10 \log \left(\frac{1}{n_{f,j}} \sum_{\omega_i \in \Omega_j} 10^{-R(\omega_i)/10} \right), \tag{16}$$

where $n_{f,j}$ denotes the number of frequencies in Ω_j. In this paper, the sound insulation is computed at the 1/24-octave band center frequencies, therefore the number of frequencies in Ω_j corresponds to 8.

3.4. Constraints

To ensure the manufacturability of the metal studs, constraints are imposed on the maximum amount of material used and on the minimal rolling angle between the web elements. Metal studs are usually produced using a technique called roll forming. The studs are formed into the desired shape by passing a metal sheet through a series of rollers. Each of these rollers deforms the sheet into its final shape. This results in a process that is suited for mass production of studs of a single shape. Small acute angles between web elements add more forming passes to the roll forming process, making the stud more expensive [29]. Therefore, the minimum absolute value of the bending angle between two web elements formed by three consecutive keypoints should be constrained. As the sheet can be bent in two directions (positive and negative rolling angle) the constraint is defined in terms of the cosine of the rolling angle θ as

$$\cos(\theta_j) = \frac{\mathbf{a}_j \cdot \mathbf{a}_{j-1}}{||\mathbf{a}_j|| \, ||\mathbf{a}_{j-1}||} \leq \cos(\theta_{\min}) \qquad \forall j \in [1, N] \tag{17}$$

with $\mathbf{a}_j = \left[x_j - x_{j-1}, y_j - y_{j-1} \right]^T$ the vector between keypoints $j - 1$ and j, and $[x_{-1}, y_{-1}] = [0\,\text{mm}, 0\,\text{mm}]$. The minimal angle between three sequential keypoints is constrained to $\theta_{\min} = 90°$. This prevents any acute angles in the design.

In order to limit the volume of sheet metal needed when producing a stud, the following constraint is imposed on the developed length of the stud's section. The length needed to form the end flanges and the lips (indicated with the thick black line in Fig. 4) is not included in the amount of material as it remains constant during the optimization process. The amount of material is computed and constrained as

$$L(\mathbf{x}) = \sum_{j=0}^{N} \sqrt{(x_{j+1} - x_j)^2 + (y_{j+1} - y_j)^2} \leq L_{\max}, \tag{18}$$

with $[x_0, y_0] = [0\,\text{mm}, 12.5\,\text{mm}]$ the coordinates of the starting point and $[x_{N+1}, y_{N+1}] = [x_N, t_{\text{cav}}/2]$ the coordinates where the web crosses at half the stud depth. The material use is constrained by $L_{\max}$, in this work a value of $L_{\max} = \frac{t_{\text{cav}} + 6W}{2}$ is adopted, yet other choices are perfectly possible.
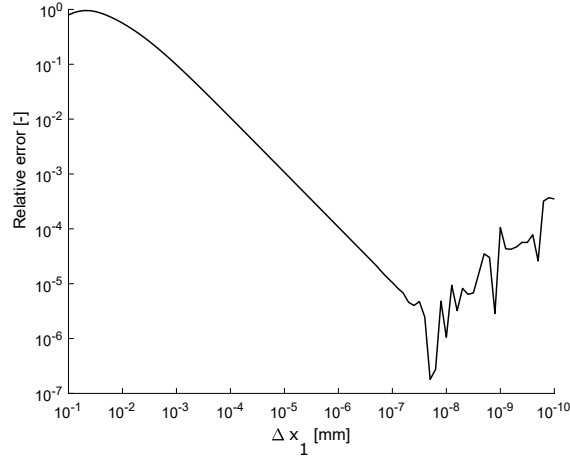
10

Figure 5: The relative error between the analytical and numerical sensitivity shows convergence up to a finite difference step of $5\mathrm{x}10^{-8}$ mm when the numerical approximation starts to diverge due to instabilities.

The metal profiles also need to comply with the relevant structural constraints. The dedicated standard EN 14353 [30] enforces tolerances on the straightness and dimensions of the profile, and requires that the stud must not buckle or deform permanently when placed onto two roller supports and loaded under its own weight. Furthermore, the standard ASTM C 754 [31] requires that the deflection of the wall under a lateral load of 240 Pa must not exceed a lateral displacement of $L_y/240$. These three mild structural constraints are verified after the optimization as they often did not limit the design space for the cross sectional shapes of the studs during optimization.

3.5. Optimization problem

The single number rating R_A, as defined in Eq. (15), is used as the objective function in the optimization, as it a suitable descriptor of the broadband sound insulation of indoor walls. The design is constrained by a minimal rolling angle and a maximal amount of material, as detailed in the previous section. This results in the following problem

$$\max_{\mathbf{x}} \quad R_A(\mathbf{x}) \tag{19}$$

$$\text{s.t.} \quad L(\mathbf{x})/L_{\max} - 1 \leq 0 \tag{20}$$

$$\cos(\theta_j(\mathbf{x})) - \cos(\theta_{\min}) \leq 0 \qquad \forall j \in [1, N] \tag{21}$$

$$0 \leq x_j \leq W \tag{22}$$

where $\mathbf{x} \in \mathbb{R}^N$ is the vector containing the design variables i.e., the horizontal coordinates of the keypoints of Fig. 4. In what follows, the optimization is performed for walls with single, double and triple sheet with a cavity depth of 50, 75, 100 or 150 mm. Gradient-based optimization is used to solve the optimization problem in Eq. (19). The sequential quadratic programming method with non-linear constraints is chosen as the optimization algorithm. An implementation in the Matlab optimization toolbox, fmincon, has been used. A multi-start approach is followed. The initial designs are chosen to be the C-shaped, Σ-shaped and M-shaped studs as shown in Fig. 1.a-c. Additionally, a fourth initial design consists of a Σ-shaped stud with an increased indentation depth of 50 mm instead of 25 mm.

The sensitivity of the objective function with respect to the design variables is elaborated in Section 3.6. The derivation of the sensitivities of the constraints with respect to the design variables is straightforward and therefore not detailed here.

11

3.6. Sensitivity analysis

The sensitivity of the single number rating R_A follows from Eq. (15) and is equal to

$$\frac{\partial R_A}{\partial x_k} = \frac{\sum_{j=1}^{16} 10^{(L_{j1} - X_j)/10} \frac{\partial X_j}{\partial x_k}}{\sum_{j=1}^{16} 10^{(L_{j1} - X_j)/10}}, \tag{23}$$

where the sensitivity of the sound insulation in 1/3 octave bands, $\frac{\partial X_j}{\partial x_k}$, follows from Eq. (16)

$$\frac{\partial X_j}{\partial x_k} = \frac{\sum_{\omega_i \in \Omega_j} 10^{R(\omega_i)/10} \frac{\partial R(\omega_i)}{\partial x_k}}{\sum_{\omega_i \in \Omega_j} 10^{R(\omega_i)10}}. \tag{24}$$

The sensitivity of the harmonic sound insulation $R(\omega)$ with respect to the design variable x_k follows from Eq. (11) and is equal to

$$\frac{\partial R}{\partial x_k} = \frac{-10}{\ln(10)\eta_{12}} \frac{\partial \eta_{12}}{\partial x_k}. \tag{25}$$

The sensitivity of the coupling loss factor η_{12} with respect to the design variables is obtained by means of a semi-analytical approach [13]: the sensitivity of the transmission loss with respect to the system matrices is computed analytically (using a direct approach) and the sensitivity of the system matrices with respect to the shape parameters is computed at element level by means of the finite difference method. The derivation of the sensitivities can be found in Appendix A. As the direct field dynamic stiffness matrices $\mathbf{D}'_{\mathrm{dir}1}$ and $\mathbf{D}'_{\mathrm{dir}2}$ do not depend on the design variables $\mathbf{x}$ in the case of the optimization of the cross-sectional shape of the metal studs in a double-leaf wall with a common frame, the result of this derivation reads

$$\frac{\partial \eta_{12}}{\partial x_k} = \frac{4}{\pi \omega n_1} \sum_{r,s} \mathrm{Re} \left(\left(-\mathbf{D}_{\mathrm{tot}}^{-T} \mathbf{A} \mathbf{C}^{T} \right)_{rs} \left(\frac{\partial \mathbf{D}'_{\mathrm{d}}}{\partial x_k} \right)_{rs} \right), \tag{26}$$

with

$$\mathbf{A} = \mathrm{Im} \left(\mathbf{D}'_{\mathrm{dir}2} \right) \text{ and } \mathbf{C} = \left(\mathbf{D}_{\mathrm{tot}}^{-1} \right) \mathrm{Im} \left(\mathbf{D}'_{\mathrm{dir}1} \right) \left(\mathbf{D}_{\mathrm{tot}}^{-1} \right)^{H}. \tag{27}$$

The sensitivity of the coupling loss factor, as computed from the above expression, has been compared against a finite difference computation for the x_1-variable in a 2x12.5/75 wall with C-shaped studs and at a frequency of 100 Hz as displayed in Fig 1.a, where x_1 refers to the horizontal coordinate of the keypoint with coordinates [3 mm, 8 mm]. The absolute value of the relative error between the analytical formulation of Eq. (26) and the finite difference computation is displayed in Fig. 5 for a step ranging from 0.1 to 10^{-10} mm. The relative error decreases for decreasing step size up to a step of $5x10^{-8}$ mm when the finite difference method becomes numerically unstable.

4. Optimization results

4.1. 50 mm cavity depth

The results for a wall with a cavity depth of 50 mm are presented in this Section. Fig. 6 and Fig. 7 show the convergence history of the objective function and the history of the maximum constraint violation for the four starting points during the optimization. Violation of the nonlinear constraints (20-21) is possible during the optimization as they are accounted for with the Lagrange multiplier technique. The maximum constraint violation is simply the largest error on each of the $N + 1$ nonlinear constraints. From the history plots, it can be concluded that the performances of the four optimized studs (corresponding to the four different starting values) is similar for double sheet while the differences are larger for single and triple sheet.

The optimized stud shapes for single, double and triple sheet are displayed in Fig. 8 together with their respective sound insulation curves. The computed sound insulation curves for walls constructed with existing stud types
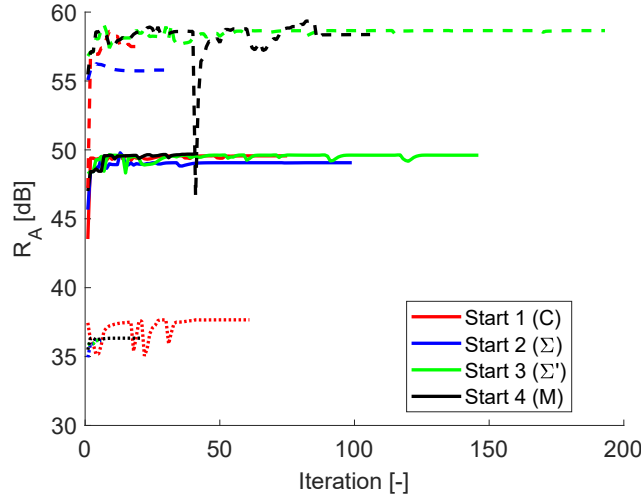
Figure 6: Convergence history of the objective function for the multistart shape optimization of the studs in a 1x12.5/50 (dotted lines), a 2x12.5/50 (solid lines) and a 3x12.5/50 wall (dashed lines).
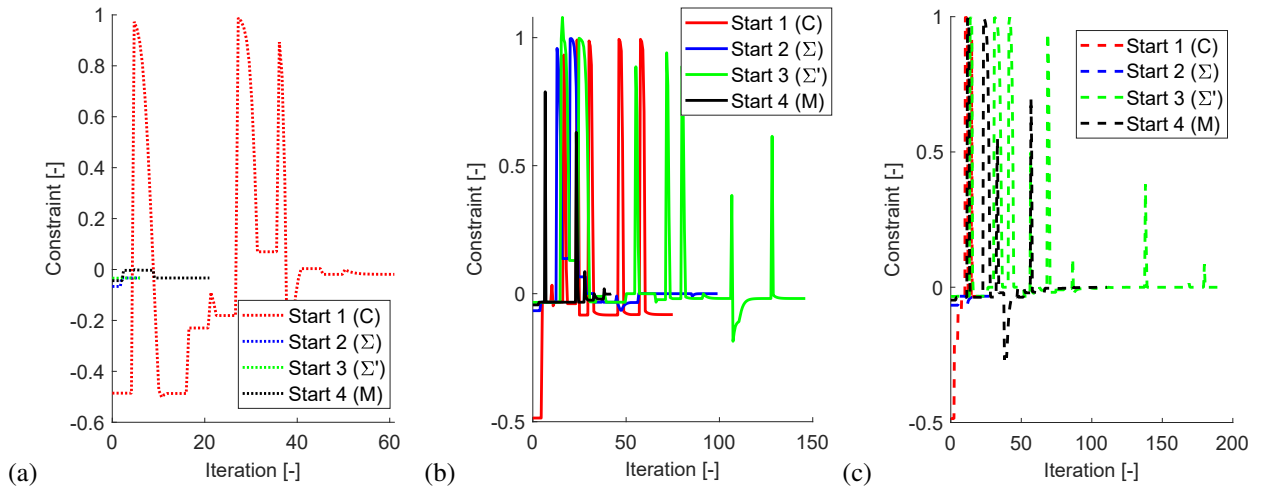

Figure 7: The maximum constraint violation for the multistart shape optimization of the studs in (a) a 1x12.5/50 (dotted lines), (b) a 2x12.5/50 (solid lines) and (c) a 3x12.5/50 wall (dashed lines).

(C-shaped, Σ-shaped and M-shaped studs as displayed in Fig. 1) and for the decoupled wall leafs are plotted for comparison. The related single number ratings are provided in the legend.

The optimized cross-sectional stud shape for a wall with single sheet resembles a C-shaped stud with four shallow indentations and one slightly deeper indentation (Fig. 8.a). This stud is a bit more flexible than the C-shaped stud due to the indentations, but is more rigid than the existing acoustic studs. This stud will better attenuate the mass-spring-mass resonance compared to a wall with decoupled wall leafs or more flexible studs. Above mass-spring-mass resonance, in the frequency range 250-500 Hz, the stud decouples the two wall leafs better than a C-shaped stud. The theoretical value of the mass-spring-mass resonance of this wall is 171 Hz and has therefore a large influence on the single number rating. This stud is optimal as it makes a trade-off between the suppression of the mass-spring-mass resonance and decoupling the wall leafs. The single number rating of this wall (37.7 dB) is therefore higher than for both the walls with a C-shaped stud frame (37.4 dB) and the decoupled leafs (35.4 dB).

The cross-sectional shape of the optimized studs for double and triple sheet are similar with respect to one another and display two deep indentations (Fig. 8.b-c). The resulting studs are more flexible compared to the existing stud
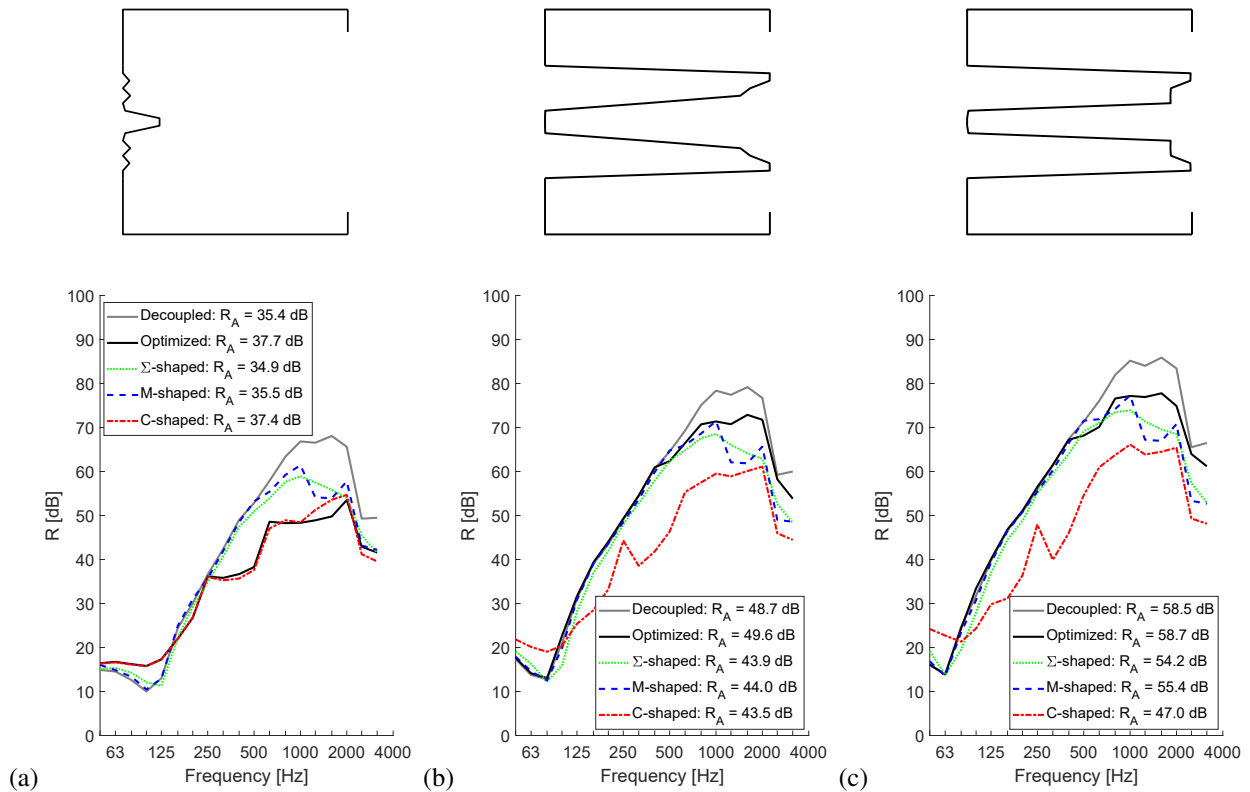
13

Figure 8: Optimized stud shape and corresponding sound insulation curve for (a) a 1x12.5/50 wall, (b) a 2x12.5/50 wall and (c) a 3x12.5/50 wall. The sound insulation of a wall with decoupled leafs and with C-shaped, Σ-shaped and M-shaped studs is also displayed.

shapes. Around mass-spring-mass resonance, the optimized studs have a performance similar to the decoupled wall and the acoustic studs while the C-shaped stud has a higher sound insulation due to the attenuation of the resonance. The single number rating for these walls is mainly determined by the sound insulation at frequencies above the mass-spring-mass resonance. The main increase in sound insulation compared to the existing studs is found above 1000 Hz. The resulting single number rating of the walls with the optimized studs (49.6 and 58.7 dB) exceeds that of the wall with decoupled leafs (48.7 and 58.5 dB) since the sound insulation in the frequency range of 100-1000 Hz is slightly higher. When compared to the currently available studs, the single number rating for the walls with the optimized stud is 6.1 and 11.7 dB higher than the C-shaped stud frame with respectively double and triple sheet, and 5.6 and 3.3 dB higher than the walls constructed with the acoustic studs with double and triple sheet.

4.2. 75 mm cavity depth

Just as for the walls with a cavity depth of 50 mm, the convergence history and the history of the maximum constraint violation have been carefully inspected. A similar convergence was found, and therefore the resulting plots are not reproduced here. The optimized stud shapes for single, double and triple sheet are displayed in Fig. 9 together with their respective sound insulation curves. The computed sound insulation curves for walls constructed with existing regular and acoustic stud types and for the decoupled wall leafs are plotted for comparison. The related single number ratings are provided in the legend.

The cross-sectional shape of the optimized studs for single and triple sheet are similar with respect to one another and display three deep indentations (Fig. 9.a and c). The cross-sectional shape of the optimized stud for double sheet displays two indentations similar to wall 3x12.5/50 (Fig. 9.b). The optimized shape for double sheet is more jagged compared to the optimal shape for wall 3x12.5/50. The main increase in sound insulation, for all three setups, compared to the existing studs can be found above 500 Hz. Similar to the walls 2x12.5/50 and 3x12.5/50, the single
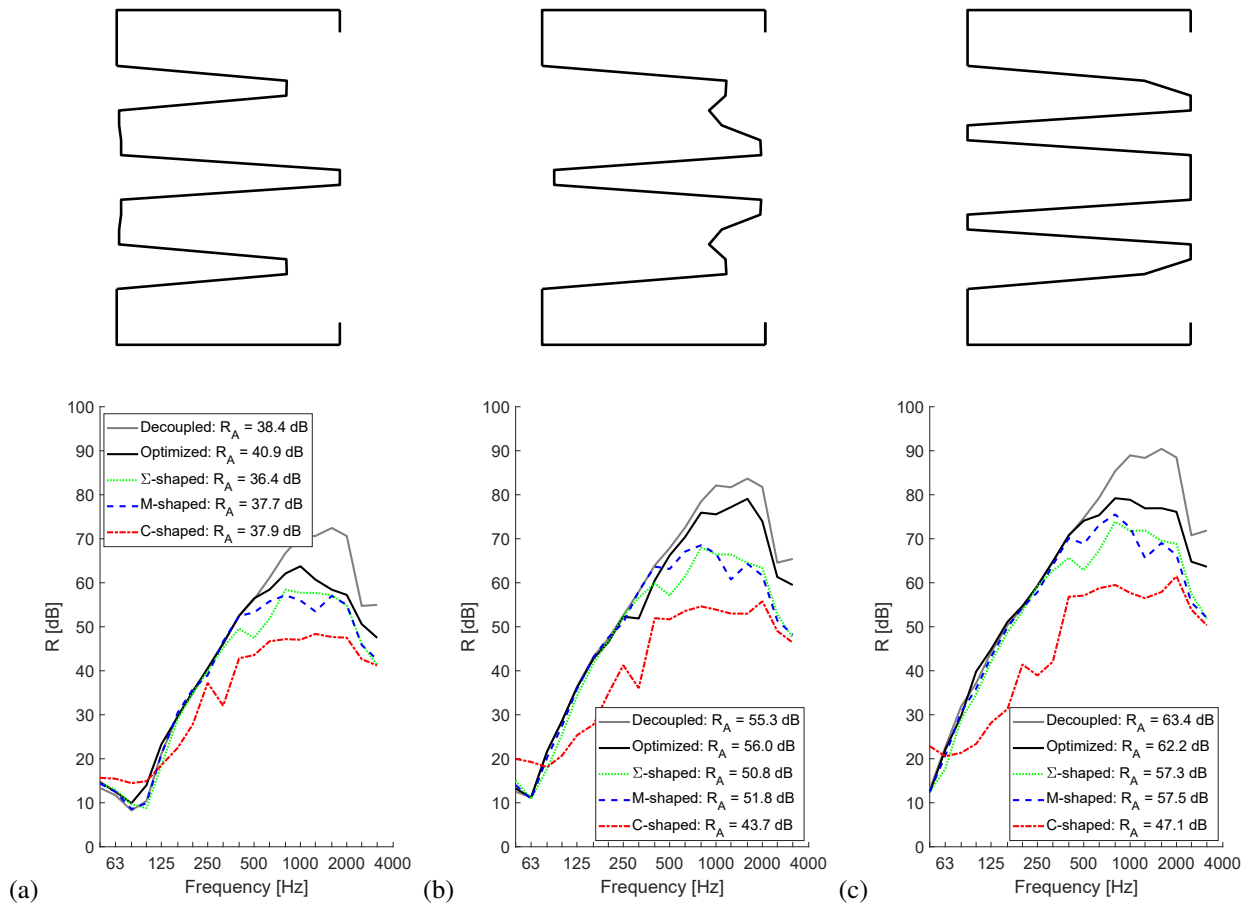
14

Figure 9: Optimized stud shape and corresponding sound insulation curve for (a) a 1x12.5/75 wall, (b) a 2x12.5/75 wall and (c) a 3x12.5/75 wall. The sound insulation of a wall with decoupled leafs and with C-shaped, Σ-shaped and M-shaped studs is also displayed.

number rating for the walls with the optimized stud exceeds even that of the decoupled wall for single and double sheet, the difference being 2.5 and 0.7 dB, respectively. For triple sheet, the single number rating is 1.2 dB lower than the wall with decoupled wall leafs. Furthermore, the single number rating for the walls with the optimized stud is 3.3, 12.3 and 15.1 dB higher than for the C-shaped studs with respectively single, double and triple sheet, and 3.5, 4.2 and 4.7 dB higher than for the existing acoustic studs.

4.3. 100 mm cavity depth

The optimized stud shapes for single, double and triple sheet are displayed in Fig. 10 together with their respective sound insulation curves. The computed sound insulation curves for walls constructed with existing regular and acoustic stud types and for the decoupled wall leafs are plotted for comparison. The related single number ratings are provided in the legend. Conversion of the optimization has been confirmed from convergence history and maximum constraint violation plots (not reproduced here).

The optimized cross-sectional shape of a metal stud for a wall with single sheet has two widely-spaced indentations (Fig. 10.a). The single number rating of the wall with single sheet (45.6 dB) exceeds that of the decoupled double wall (43.8 dB). The better performance relates to the 1/3 octave band of 100 Hz, where the sound insulation of the wall with the optimized stud is 5.8 dB higher than for the decoupled wall. The cross-sectional shapes of the optimized studs for double and triple sheet are similar with respect to one another and feature two wide, jagged indentations (Fig. 10.b-c). The main gain in sound insulation, when compared to the available acoustic studs, is found in the frequency range above 315 Hz. The single number rating for the walls with the optimized stud is 7.6, 15.2 and 18.8 dB higher than the
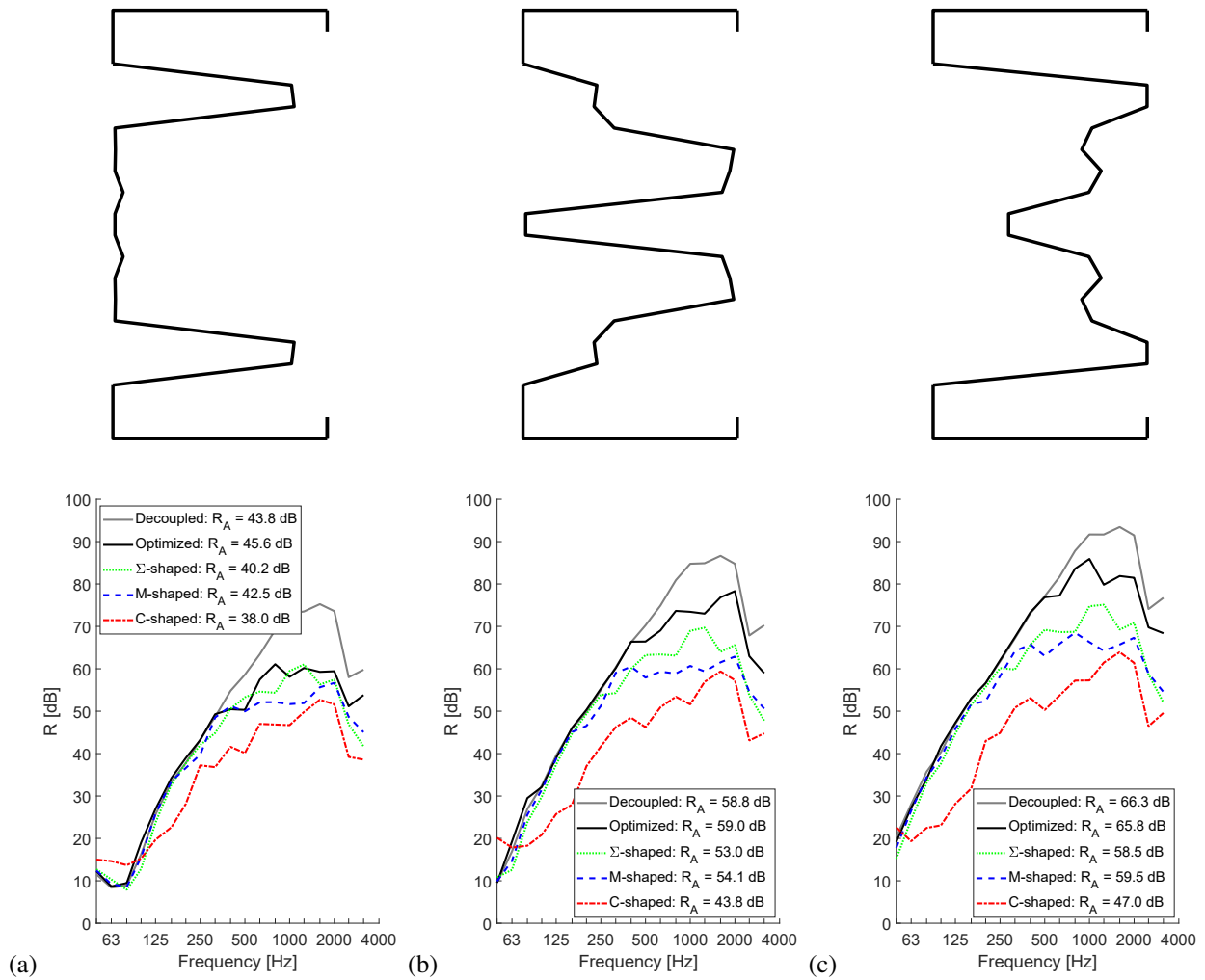
15

Figure 10: Optimized stud shape and corresponding sound insulation curve for (a) a 1x12.5/100 wall, (b) a 2x12.5/100 wall and (c) a 3x12.5/100 wall. The sound insulation of a wall with decoupled leafs and with C-shaped, Σ-shaped and M-shaped studs is also displayed.

C-shaped stud frame with respectively single, double and triple sheet, and 3.1, 4.9 and 6.3 dB higher than the walls constructed with the existing acoustic studs.

4.4. 150 mm cavity depth

The optimized stud shapes for single, double and triple sheet are displayed in Fig. 11 together with their respective sound insulation curves. The computed sound insulation curves for walls constructed with existing regular and acoustic stud types and for the decoupled wall leafs are plotted for comparison. The related single number ratings are provided in the legend. Conversion of the optimization has been confirmed from convergence history and maximum constraint violation plots (not reproduced here).

The cross-sectional shape of the optimized studs for single, double and triple sheet exhibits two indentations (Fig. 11), similar to the optimized studs for a 3x12.5/100 wall (Fig. 10.c). The single number rating for the walls with the optimized stud is 11.6, 18.3 and 21.9 dB higher than the C-shaped stud frame with respectively single, double and triple sheet, and 5.3, 8.4 and 10.4 dB higher than the walls constructed with existing acoustic studs. The very substantial improvement with respect to the existing acoustic studs is due to a consistently higher performance in the broad frequency range of 250-1250 Hz.
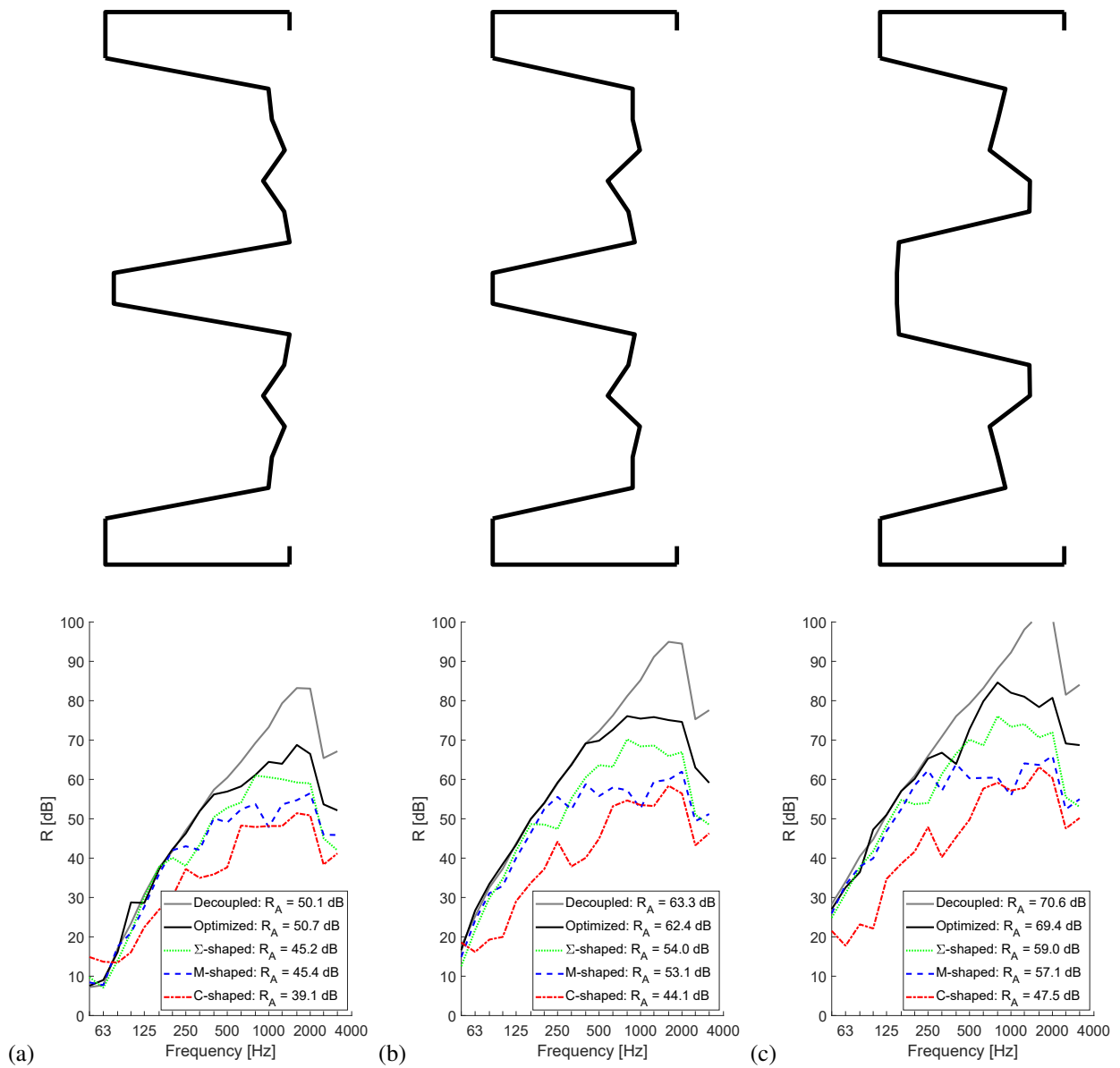
Figure 11: Optimized stud shape and corresponding sound insulation curve for (a) a 1x12.5/150 wall, (b) a 2x12.5/150 wall and (c) a 3x12.5/150 wall. The sound insulation of a wall with decoupled leafs and with C-shaped, Σ-shaped and M-shaped studs is also displayed.
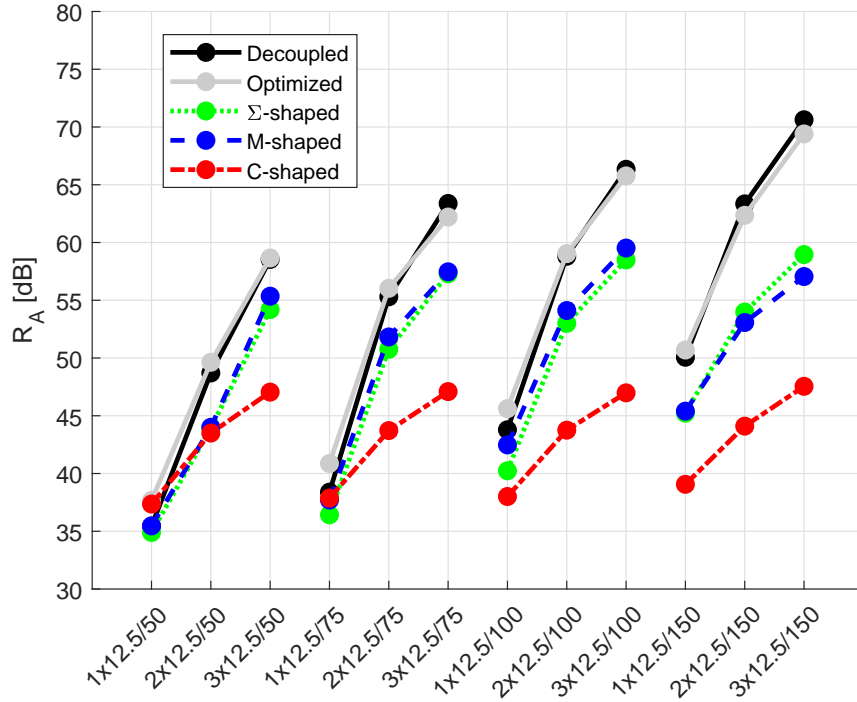
Figure 12: Comparison of the single number rating R_A for all 12 wall setups with 5 different stud frames.

5. Discussion

A comparison of the single number rating for all 12 wall types with a C-shaped stud frame, a M-shaped stud frame, a Σ-shapes stud frame, the optimized stud frame and a wall with decoupled wall leafs is presented in Fig. 12. The walls with an M-shaped stud frame and Σ-shaped stud frame have a very similar performance, as can be observed from the blue and green curves in Fig. 12. The walls with the optimized studs have a similar performance compared to walls with decoupled leafs as can be seen from the black and gray curves in Fig. 12. The gain in single number rating, R_A, when compared to a C-shaped stud frame is 11.8 dB on average, with a maximum of 21.9 dB for wall 3x12.5/150. Compared to the existing acoustic studs the gain is 5.1 dB on average, with a maximum of 10.4 dB for wall 3x12.5/150. The C-shaped stud frame has the lowest single number rating R_A for all setups except for 1x12.5/50 and 1x12.5/75, for which the mass-spring-mass resonance has a large influence on the single number rating. For increasing cavity depth, the single number rating of the walls with a C-shaped stud frame remains almost constant. This has also been observed in experimental studies such as the one by Vermeir and Gerretsen [**?**].

Interestingly, the optimized studs in combination with double sheet outperform the existing acoustic studs with triple sheet for the same total wall thickness. This can be observed for 2x12.5/75 (opt.) vs. 3x12.5/50 (Σ/M) and for 2x12.5/100 (opt.) vs. 3x12.5/75 (Σ/M). This indicates that a substantial weight (and cost) reduction could be achieved without changing the wall thickness nor the sound insulation performance.

As discussed in section 3.4, the relevant structural constraints are very mild and therefore they are verified after optimization. According to EN 14353 [30], a stud must not deform permanently or buckle under its own weight when placed on two roller supports spaced at 1.5 m width. For each optimized stud, the maximal allowed stresses in the stud under its own weight, $\sigma_{v,max}$, and the torsional buckling load, $P_{buckling}$, have been computed in the Ansys finite element software. The results are presented in Table 2. When compared to the yield strength, σ_{yield}, and the self weight of the studs, P_{self}, none of the studs will plastically deform or buckle under their own weight when placed onto the two supports. According to ASTM C 754 – 18 [31], the deflection of a non-load bearing wall under a uniform lateral pressure of 240 Pa must not exceed $L_y/240$ with L_y the height of the wall (2.95 m in the present analysis). The

Setup	$\sigma_{v,max}/\sigma_{yield}$ [%]	$P_{self}/P_{buckling}$ [%]	$d_{max}/(L_y/240)$ [%]
1x12.5/50	7.0	1.2	42.2
2x12.5/50	22.5	3.5	48.1
3x12.5/50	22.9	3.6	40.1
1x12.5/75	24.0	4.0	35.1
2x12.5/75	24.6	3.6	29.6
3x12.5/75	30.8	4.7	28.0
1x12.5/100	18.7	4.8	46.1
2x12.5/100	22.3	4.9	23.4
3x12.5/100	26.1	4.7	34.6
1x12.5/150	31.5	9.3	46.9
2x12.5/150	24.9	8.4	31.6
3x12.5/150	22.6	8.3	28.9

Table 2: Maximal stress compared to the yield strength and self weight compared to the torsional buckling load for the optimized stud, placed on two roller supports spaced 1.5 m apart, and maximal deflection of the wall subjected to a uniform lateral load of 240 Pa, compared to the maximum allowed displacement.

maximal displacement under a static uniform load, d_{max}, is computed using the Ansys finite element software. The deflections remain far below the maximum allowed (see Table 2).

6. Conclusions

The design optimization of vibro-acoustic systems over a large frequency band within the hybrid Det-SEA framework has been considered. The sensitivities of the sound insulation to the cross-sectional stud shape parameters were obtained in a semi-analytic way. To increase the computational efficiency, the resulting sensitivities were rearranged as the product of terms that only depend on the state of the system and the sensitivities of the system matrices, such that the sensitivities of the sound insulation can be obtained in a computationally efficient way. The sequential quadratic programming method with non-linear constraints has been used for the optimization.

As an example of the proposed methodology, the cross-sectional shape of flexible metal studs in double-leaf plasterboard walls has been optimized for the overall A-weighted sound reduction under pink noise excitation. In order to obtain practically feasible designs in terms of material usage and manufacturing limitations, inequality constraints have been incorporated in the optimization procedure. The relevant constraints related to strength and stiffness of the wall are very mild and therefore verified after optimization. Although the focus in this paper is on the shape optimization of the broadband sound insulation rating R_A for symmetric studs, the approach can be readily generalized to other performance indicators such as R_W, other parametrization schemes and other wall types.

The sound insulation prediction model that has been employed in the optimization procedure has been validated previously for plasterboard walls with conventional C-shaped studs. Additional validations on plasterboard walls with acoustic studs have been performed in the present work. They confirm the accuracy of the prediction model also for walls with very flexible studs and therefore provide confidence in the validity of the optimization results.

The optimized studs exhibit a significantly higher sound insulation than conventional C-shaped studs and existing acoustic studs, with an average gain in single number rating R_A of 11.8 dB and 5.1 dB, respectively. The optimized designs are more flexible compared to existing studs which results in a weaker structural coupling, except for wall setup 1x12.5/50. The exception occurs when the mass-spring-mass resonance greatly influences the single number rating and this resonance is better attenuated by a less flexible stud.

Appendix A. Sensitivity of the coupling loss factor

The coupling loss factor η_{12} between the SEA subsystems 1 and 2 is defined as [8]

$$\eta_{12} = \frac{2}{\pi \omega n_1} \sum_{r,s} \tilde{\mathbf{D}}'_{\text{dir}2,rs} \left(\mathbf{D}_{\text{tot}}^{-1} \tilde{\mathbf{D}}'_{\text{dir}1} \mathbf{D}_{\text{tot}}^{-H} \right)_{rs}. \tag{A.1}$$

with

$$\tilde{\mathbf{D}}'_{\text{dir}1,rs} := \text{Im}\left(\mathbf{D}'_{\text{dir}1,rs} \right) \text{ and } \tilde{\mathbf{D}}'_{\text{dir}2,rs} := \text{Im}\left(\mathbf{D}'_{\text{dir}2,rs} \right) \tag{A.2}$$

Taking the derivative of the coupling loss factor with respect to a variable x_i gives

$$\frac{\partial \eta_{12}}{\partial x_j} = \frac{2}{\pi \omega n_1} \sum_{r,s} \left[\tilde{\mathbf{D}}'_{\text{dir}2,rs} \left(\frac{\partial \mathbf{D}_{\text{tot}}^{-1}}{\partial x_j} \tilde{\mathbf{D}}'_{\text{dir}1} \mathbf{D}_{\text{tot}}^{-H} + \mathbf{D}_{\text{tot}}^{-1} \tilde{\mathbf{D}}'_{\text{dir}1} \frac{\partial \mathbf{D}_{\text{tot}}^{-H}}{\partial x_j} \right)_{rs} + \frac{\partial \tilde{\mathbf{D}}'_{\text{dir}2,rs}}{\partial x_j} \left(\mathbf{D}_{\text{tot}}^{-1} \tilde{\mathbf{D}}'_{\text{dir}1} \mathbf{D}_{\text{tot}}^{-H} \right)_{rs} + \tilde{\mathbf{D}}'_{\text{dir}2,rs} \left(\mathbf{D}_{\text{tot}}^{-1} \frac{\partial \tilde{\mathbf{D}}'_{\text{dir}1}}{\partial x_j} \mathbf{D}_{\text{tot}}^{-H} \right) \right.$$
$$\tag{A.3}$$

$$= \left(\frac{\partial \eta_{12}}{\partial x_j} \right)_1 + \left(\frac{\partial \eta_{12}}{\partial x_j} \right)_2 + \left(\frac{\partial \eta_{12}}{\partial x_j} \right)_3 \tag{A.4}$$

with

$$\left(\frac{\partial \eta_{12}}{\partial x_j} \right)_1 := \frac{2}{\pi \omega n_1} \sum_{r,s} \tilde{\mathbf{D}}'_{\text{dir}2,rs} \left(\frac{\partial \mathbf{D}_{\text{tot}}^{-1}}{\partial x_j} \tilde{\mathbf{D}}'_{\text{dir}1} \mathbf{D}_{\text{tot}}^{-H} + \mathbf{D}_{\text{tot}}^{-1} \tilde{\mathbf{D}}'_{\text{dir}1} \frac{\partial \mathbf{D}_{\text{tot}}^{-H}}{\partial x_j} \right)_{rs}, \tag{A.5}$$

$$\left(\frac{\partial \eta_{12}}{\partial x_j} \right)_2 := \frac{2}{\pi \omega n_1} \sum_{r,s} \frac{\partial \tilde{\mathbf{D}}'_{\text{dir}2,rs}}{\partial x_j} \left(\mathbf{D}_{\text{tot}}^{-1} \tilde{\mathbf{D}}'_{\text{dir}1} \mathbf{D}_{\text{tot}}^{-H} \right)_{rs}, \tag{A.6}$$

$$\left(\frac{\partial \eta_{12}}{\partial x_j} \right)_3 := \frac{2}{\pi \omega n_1} \sum_{r,s} \tilde{\mathbf{D}}'_{\text{dir}2,rs} \left(\mathbf{D}_{\text{tot}}^{-1} \frac{\partial \tilde{\mathbf{D}}'_{\text{dir}1}}{\partial x_j} \mathbf{D}_{\text{tot}}^{-H} \right)_{rs}. \tag{A.7}$$

$$\tag{A.8}$$

The derivative is split up into three terms. The first term, $\left(\frac{\partial \eta_{12}}{\partial x_j} \right)_1$, depends on the sensitivity of the total dynamic stiffness matrix $\mathbf{D}_{\text{tot}}$. The second term, $\left(\frac{\partial \eta_{12}}{\partial x_j} \right)_2$, depends on the direct field dynamic stiffness matrix of the second SEA subsystem $\mathbf{D}_{\text{dir}2}$ and the third term, $\left(\frac{\partial \eta_{12}}{\partial x_j} \right)_3$, depends on the direct field dynamic stiffness matrix of the first SEA subsystem $\mathbf{D}_{\text{dir}1}$. These three parts are elaborated separately in what follows. In this analysis it is assumed that the direct field dynamic stiffness matrices $\mathbf{D}_{\text{dir}1}$ and $\mathbf{D}_{\text{dir}2}$ in terms of the physical coordinates of the deterministic subsystem do not depend on the design variables $\mathbf{x}$ and that these design variables $\mathbf{x}$ only assume real values.

Appendix A.1. Properties of the element-wise product

Lemma:
The sum over all elements of the element-wise product of a matrix $\mathbf{A}$ and a matrix product $\mathbf{BC}$ is equal to the sum over all elements of the element-wise product of the matrix product $\mathbf{AC}^{\text{T}}$ and the matrix $\mathbf{B}$.

$$\sum_{r,s} \mathbf{A}_{rs}(\mathbf{BC})_{rs} = \sum_{r,s} (\mathbf{AC}^{\text{T}})_{rs} \mathbf{B}_{rs} \tag{A.9}$$

The previous lemma holds for all matrices $\mathbf{A}$ of size [a,b], $\mathbf{B}$ of size [a,c] and $\mathbf{C}$ of size [c,b].

Proof:

$$\sum_{r,s}(\mathbf{A}\mathbf{C}^{\mathrm{T}})_{rs}\mathbf{B}_{rs} = \sum_{rsq}\mathbf{A}(r,q)\mathbf{C}(s,q)\mathbf{B}(r,s) \tag{A.10}$$

$$= \sum_{rsq}\mathbf{A}(r,q)\mathbf{B}(r,s)\mathbf{C}(s,q) \tag{A.11}$$

$$= \sum_{rq}\mathbf{A}_{rq}\left(\mathbf{B}\mathbf{C}\right)_{rq}. \tag{A.12}$$

Appendix A.2. Terms depending on the sensitivity of the total dynamic stiffness matrix

The first term of the derivative, i.e. the part that depends on the sensitivity $\frac{\partial \mathbf{D}_{\mathrm{tot}}}{\partial x_j}$, can be elaborated using the properties of the derivative of the inverse of a matrix [32] as

$$\left(\frac{\partial \eta_{12}}{\partial x_j}\right)_1 := \frac{2}{\pi \omega n_1}\sum_{r,s}\tilde{\mathbf{D}}'_{\mathrm{dir2},rs}\left(\frac{\partial \mathbf{D}_{\mathrm{tot}}^{-1}}{\partial x_j}\tilde{\mathbf{D}}'_{\mathrm{dir1}}\mathbf{D}_{\mathrm{tot}}^{-\mathrm{H}} + \mathbf{D}_{\mathrm{tot}}^{-1}\tilde{\mathbf{D}}'_{\mathrm{dir1}}\frac{\partial \mathbf{D}_{\mathrm{tot}}^{-\mathrm{H}}}{\partial x_j}\right)_{rs} \tag{A.13}$$

$$= \frac{2}{\pi \omega n_1}\sum_{r,s}\tilde{\mathbf{D}}'_{\mathrm{dir2},rs}\left(-\mathbf{D}_{\mathrm{tot}}^{-1}\frac{\partial \mathbf{D}_{\mathrm{tot}}}{\partial x_j}\mathbf{D}_{\mathrm{tot}}^{-1}\tilde{\mathbf{D}}'_{\mathrm{dir1}}\mathbf{D}_{\mathrm{tot}}^{-\mathrm{H}} - \mathbf{D}_{\mathrm{tot}}^{-1}\tilde{\mathbf{D}}'_{\mathrm{dir1}}\mathbf{D}_{\mathrm{tot}}^{-\mathrm{H}}\frac{\partial \mathbf{D}_{\mathrm{tot}}^{\mathrm{H}}}{\partial x_j}\mathbf{D}_{\mathrm{tot}}^{-\mathrm{H}}\right)_{rs} \tag{A.14}$$

$$= \frac{2}{\pi \omega n_1}\sum_{r,s}\mathbf{A}_{rs}(\mathbf{B}\mathbf{C} + \mathbf{C}\mathbf{B}^{\mathrm{H}})_{rs} \tag{A.15}$$

with

$$\mathbf{A} := \mathrm{Im}\left(\mathbf{D}'_{\mathrm{dir2}}\right),\ \mathbf{B} := -\mathbf{D}_{\mathrm{tot}}^{-1}\frac{\partial \mathbf{D}_{\mathrm{tot}}}{\partial x_j}\ \text{and}\ \mathbf{C} := \mathbf{D}_{\mathrm{tot}}^{-1}\tilde{\mathbf{D}}'_{\mathrm{dir1}}\mathbf{D}_{\mathrm{tot}}^{-\mathrm{H}} \tag{A.16}$$

This can be elaborated as

$$\left(\frac{\partial \eta_{12}}{\partial x_j}\right)_1 = \frac{2}{\pi \omega n_1}\sum_{r,s}\mathbf{A}_{rs}(\mathbf{B}\mathbf{C})_{rs} + \mathbf{A}_{rs}(\mathbf{C}\mathbf{B}^{\mathrm{H}})_{rs} \tag{A.17}$$

$$= \frac{2}{\pi \omega n_1}\sum_{r,s}\mathbf{A}_{rs}(\mathbf{B}\mathbf{C})_{rs} + \mathbf{A}_{rs}^{\mathrm{T}}((\mathbf{C}\mathbf{B}^{\mathrm{H}})^{\mathrm{T}})_{rs} \tag{A.18}$$

$$= \frac{2}{\pi \omega n_1}\sum_{r,s}\mathbf{A}_{rs}(\mathbf{B}\mathbf{C})_{rs} + \mathbf{A}_{rs}^{\mathrm{T}}((\mathrm{conj}(\mathbf{B})\mathbf{C}^{\mathrm{T}})_{rs}. \tag{A.19}$$

Using Property (A.9), the sensitivity becomes

$$\left(\frac{\partial \eta_{12}}{\partial x_j}\right)_1 = \frac{2}{\pi \omega n_1}\sum_{r,s}(\mathbf{A}\mathbf{C}^{\mathrm{T}})_{rs}\mathbf{B}_{rs} + (\mathbf{A}\mathbf{C})_{rs}\mathrm{conj}(\mathbf{B})_{rs}. \tag{A.20}$$

The conjugate transpose $\mathbf{C}^{\mathrm{H}}$ is equal to $\mathbf{C}$ since $(\tilde{\mathbf{D}}'_{\mathrm{dir1}})^{\mathrm{H}} = \tilde{\mathbf{D}}'_{\mathrm{dir1}}$ because $\mathbf{D}'_{\mathrm{dir1}}$ is a symmetric matrix.

$$\mathbf{C}^{\mathrm{H}} = \left(\mathbf{D}_{\mathrm{tot}}^{-1}\tilde{\mathbf{D}}'_{\mathrm{dir1}}\mathbf{D}_{\mathrm{tot}}^{-\mathrm{H}}\right)^{\mathrm{H}}$$

$$= \mathbf{D}_{\mathrm{tot}}^{-1}(\tilde{\mathbf{D}}'_{\mathrm{dir1}})^{\mathrm{H}}\mathbf{D}_{\mathrm{tot}}^{-\mathrm{H}}$$

$$= \mathbf{D}_{\mathrm{tot}}^{-1}\tilde{\mathbf{D}}'_{\mathrm{dir1}}\mathbf{D}_{\mathrm{tot}}^{-\mathrm{H}}$$

$$= \mathbf{C}, \tag{A.21}$$

Using Property (A.21),the sensitivity becomes

$$\left(\frac{\partial \eta_{12}}{\partial x_j}\right)_1 = \frac{2}{\pi \omega n_1}\sum_{r,s}(\mathbf{A}\mathbf{C}^{\mathrm{T}})_{rs}\mathbf{B}_{rs} + (\mathbf{A}\mathbf{C}^{\mathrm{H}})_{rs}\mathrm{conj}(\mathbf{B})_{rs}. \tag{A.22}$$

21

By decomposing each term of these element wise products into a real and an imaginary part, this equation becomes

$$\left(\frac{\partial \eta_{12}}{\partial x_j}\right)_1 = \frac{2}{\pi\omega n_1}\sum_{r,s}\left(\mathrm{Re}(\mathbf{AC}^{\mathrm{T}}) + \mathrm{i}\,\mathrm{Im}(\mathbf{AC}^{\mathrm{T}})\right)_{rs}(\mathrm{Re}(\mathbf{B}) + \mathrm{i}\,\mathrm{Im}(\mathbf{B}))_{rs} + \left(\mathrm{Re}(\mathbf{AC}^{\mathrm{H}}) + \mathrm{i}\,\mathrm{Im}(\mathbf{AC}^{\mathrm{H}})\right)_{rs}(\mathrm{Re}(\mathrm{conj}(\mathbf{B}))) + \mathrm{i}\,\mathrm{Im}(\mathrm{conj}(\mathbf{B}))$$

(A.23)

$$= \frac{2}{\pi\omega n_1}\sum_{r,s}\left(\mathrm{Re}(\mathbf{AC}^{\mathrm{T}}) + \mathrm{i}\,\mathrm{Im}(\mathbf{AC}^{\mathrm{T}})\right)_{rs}(\mathrm{Re}(\mathbf{B}) + \mathrm{i}\,\mathrm{Im}(\mathbf{B}))_{rs} + \left(\mathrm{Re}(\mathbf{AC}^{\mathrm{T}}) - \mathrm{i}\,\mathrm{Im}(\mathbf{AC}^{\mathrm{T}})\right)_{rs}(\mathrm{Re}(\mathbf{B})) - i\mathrm{Im}(\mathbf{B})))_{rs}$$

(A.24)

as

$$\mathrm{Re}(\mathbf{AC}^{H}) = \mathbf{A}\mathrm{Re}(\mathbf{C}^{H}) = \mathbf{A}\mathrm{Re}(\mathbf{C}^{\mathrm{T}}) = \mathrm{Re}(\mathbf{AC}^{\mathrm{T}})$$

(A.25)

$$\mathrm{Im}(\mathbf{AC}^{H}) = \mathbf{A}\mathrm{Im}(\mathbf{C}^{H}) = -\mathbf{A}\mathrm{Im}(\mathbf{C}^{\mathrm{T}}) = -\mathrm{Im}(\mathbf{AC}^{\mathrm{T}}).$$

(A.26)

By grouping terms the final result becomes

$$\left(\frac{\partial \eta_{12}}{\partial x_j}\right)_1 = \frac{4}{\pi\omega n_1}\sum_{r,s}\mathrm{Re}((\mathbf{AC}^{\mathrm{T}})_{rs}\mathbf{B}_{rs})$$

(A.27)

$$= \frac{4}{\pi\omega n_1}\mathrm{Re}\left(\sum_{r,s}(\mathbf{AC}^{\mathrm{T}})_{rs}\mathbf{B}_{rs}\right),$$

(A.28)

or alternatively, using Property (A.9)

$$\left(\frac{\partial \eta_{12}}{\partial x_j}\right)_1 = \frac{4}{\pi\omega n_1}\mathrm{Re}\left(\sum_{r,s}(-\mathbf{D}_{\mathrm{tot}}^{-T}\mathbf{AC}^{\mathrm{T}})_{rs}\left(\frac{\partial \mathbf{D}_{\mathrm{tot}}}{\partial x_j}\right)_{rs}\right).$$

(A.29)

Appendix A.3. Terms depending on the sensitivity of the direct field dynamic stiffness matrix of subsystem 2

The direct field dynamic stiffness matrix $\mathbf{D}'_{\mathrm{dir}2}$ is defined as

$$\mathbf{D}'_{\mathrm{dir}2} = \boldsymbol{\phi}_{\mathbf{2}}^{\mathrm{T}}\mathbf{D}_{\mathrm{dir}2}\boldsymbol{\phi}_{\mathbf{2}}$$

(A.30)

with $\boldsymbol{\phi}_{\mathbf{2}}$ the eigenvectors, used as a modal basis to describe the vibration field of the deterministic subsystem, of the part that is in contact with the second SEA subsystem; $\mathbf{D}_{\mathrm{dir}2}$ is the direct field dynamic stiffness matrix of the second SEA subsystem in terms of the physical coordinates of the deterministic subsystem.

Assuming that the design variables $\mathbf{x}$ are real values, the derivative of the imaginary part can be written as

$$\left(\frac{\partial \eta_{12}}{\partial x_j}\right)_2 := \frac{2}{\pi\omega n_1}\sum_{r,s}\frac{\partial \tilde{\mathbf{D}}'_{\mathrm{dir}2,rs}}{\partial x_j}\mathbf{C}_{rs}$$

(A.31)

$$= \frac{2}{\pi\omega n_1}\sum_{r,s}\mathrm{Im}\left(\frac{\partial \mathbf{D}'_{\mathrm{dir}2,rs}}{\partial x_j}\right)\mathbf{C}_{rs}$$

(A.32)

$$= \frac{2}{\pi\omega n_1}\sum_{r,s}\mathrm{Im}\left(\frac{\partial \boldsymbol{\phi}_2^{\mathrm{T}}}{\partial x_j}\mathbf{D}_{\mathrm{dir}2}\boldsymbol{\phi}_2 + \boldsymbol{\phi}_2^{\mathrm{T}}\mathbf{D}_{\mathrm{dir}2}\frac{\partial \boldsymbol{\phi}_2}{\partial x_j}\right)_{rs}\mathbf{C}_{rs}.$$

(A.33)

This can be written as

$$\left(\frac{\partial \eta_{12}}{\partial x_j}\right)_2 = \frac{2}{\pi\omega n_1}\sum_{r,s}\mathbf{C}_{rs}\mathrm{Im}\left(\mathbf{F}^{\mathrm{T}}\mathbf{E} + \mathbf{E}^{\mathrm{T}}\mathbf{F}\right)_{rs}$$

(A.34)

22

with

$$\mathbf{E} := \mathbf{D}_{\mathrm{dir2}}\phi_2 \text{ and } \mathbf{F} := \frac{\partial \phi_2}{\partial x_j} \tag{A.35}$$

The imaginary part of the matrix product can be written as the product of the imaginary and real parts as

$$\left(\frac{\partial \eta_{12}}{\partial x_j}\right)_2 = \frac{2}{\pi \omega n_1} \sum_{r,s} \mathbf{C}_{rs} \left(\mathrm{Re}(\mathbf{F}^{\mathrm{T}})\mathrm{Im}(\mathbf{E}) + \mathrm{Im}(\mathbf{F}^{\mathrm{T}})\mathrm{Re}(\mathbf{E}) + \mathrm{Re}(\mathbf{E}^{\mathrm{T}})\mathrm{Im}(\mathbf{F}) + \mathrm{Im}(\mathbf{E}^{\mathrm{T}})\mathrm{Re}(\mathbf{F})\right)_{rs} \tag{A.36}$$

Using Property (A.9), the sensitivity becomes

$$\left(\frac{\partial \eta_{12}}{\partial x_j}\right)_2 = \frac{2}{\pi \omega n_1} \sum_{r,s} (\mathbf{C}\,\mathrm{Im}(\mathbf{E}^{\mathrm{T}}))_{rs}\mathrm{Re}(\mathbf{F}^{\mathrm{T}})_{rs} + (\mathbf{C}\,\mathrm{Re}(\mathbf{E}^{\mathrm{T}}))_{rs}\mathrm{Im}(\mathbf{F}^{\mathrm{T}})_{rs} + \mathbf{C}_{rs}\left(\mathrm{Re}(\mathbf{E}^{\mathrm{T}})\mathrm{Im}(\mathbf{F}) + \mathrm{Im}(\mathbf{E}^{\mathrm{T}})\mathrm{Re}(\mathbf{F})\right)_{rs} \tag{A.37}$$

$$= \frac{2}{\pi \omega n_1} \sum_{r,s} (\mathbf{C}\,\mathrm{Im}(\mathbf{E}^{\mathrm{T}}))_{rs}\mathrm{Re}(\mathbf{F}^{\mathrm{T}})_{rs} + (\mathbf{C}\,\mathrm{Re}(\mathbf{E}^{\mathrm{T}}))_{rs}\mathrm{Im}(\mathbf{F}^{\mathrm{T}})_{rs} + (\mathbf{C}^{\mathrm{T}})_{rs}\left(\mathrm{Re}(\mathbf{F}^{\mathrm{T}})\mathrm{Im}(\mathbf{E}) + \mathrm{Im}(\mathbf{F}^{\mathrm{T}})\mathrm{Re}(\mathbf{E})\right)_{rs} \tag{A.38}$$

$$= \frac{2}{\pi \omega n_1} \sum_{r,s} (\mathbf{C}\,\mathrm{Im}(\mathbf{E}^{\mathrm{T}}))_{rs}\mathrm{Re}(\mathbf{F}^{\mathrm{T}})_{rs} + (\mathbf{C}\,\mathrm{Re}(\mathbf{E}^{\mathrm{T}}))_{rs}\mathrm{Im}(\mathbf{F}^{\mathrm{T}})_{rs} + (\mathbf{C}^{\mathrm{T}}\,\mathrm{Im}(\mathbf{E}^{\mathrm{T}}))_{rs}\mathrm{Re}(\mathbf{F}^{\mathrm{T}})_{rs} + (\mathbf{C}^{\mathrm{T}}\,\mathrm{Re}(\mathbf{E}^{\mathrm{T}}))_{rs}\mathrm{Im}(\mathbf{F}^{\mathrm{T}})_{rs} \tag{A.39}$$

$$= \frac{2}{\pi \omega n_1} \sum_{r,s} (\mathrm{Im}(\mathbf{E})\mathbf{C}^{\mathrm{T}})_{rs}\mathrm{Re}(\mathbf{F})_{rs} + (\mathrm{Re}(\mathbf{E})\mathbf{C}^{\mathrm{T}}))_{rs}\mathrm{Im}(\mathbf{F})_{rs} + (\mathrm{Im}(\mathbf{E})\mathbf{C})_{rs}\mathrm{Re}(\mathbf{F})_{rs} + (\mathrm{Re}(\mathbf{E})\,\mathbf{C})_{rs}\mathrm{Im}(\mathbf{F})_{rs} \tag{A.40}$$

$$= \frac{2}{\pi \omega n_1} \sum_{r,s} (\mathrm{Im}(\mathbf{E})(\mathbf{C} + \mathbf{C}^{\mathrm{T}}))_{rs}\mathrm{Re}(\mathbf{F})_{rs} + (\mathrm{Re}(\mathbf{E})(\mathbf{C} + \mathbf{C}^{\mathrm{T}}))_{rs}\mathrm{Im}(\mathbf{F})_{rs} \tag{A.41}$$

Using Property (A.21), the sensitivity becomes

$$\left(\frac{\partial \eta_{12}}{\partial x_j}\right)_2 = \frac{2}{\pi \omega n_1} \sum_{r,s} (\mathrm{Im}(\mathbf{E})(\mathbf{C} + \mathrm{conj}(\mathbf{C})))_{rs}\mathrm{Re}(\mathbf{F})_{rs} + (\mathrm{Re}(\mathbf{E})(\mathbf{C} + \mathrm{conj}(\mathbf{C})))_{rs}\mathrm{Im}(\mathbf{F})_{rs} \tag{A.42}$$

$$= \frac{2}{\pi \omega n_1} \sum_{r,s} (\mathrm{Im}(\mathbf{E})(2\,\mathrm{Re}(\mathbf{C})))_{rs}\mathrm{Re}(\mathbf{F})_{rs} + (\mathrm{Re}(\mathbf{E})(2\,\mathrm{Re}(\mathbf{C})))_{rs}\mathrm{Im}(\mathbf{F})_{rs} \tag{A.43}$$

$$= \frac{4}{\pi \omega n_1}\mathrm{Im}\left(\sum_{r,s} (\mathbf{E}\,\mathrm{Re}(\mathbf{C}))_{rs}\mathbf{F}_{rs}\right). \tag{A.44}$$

Or alternatively, with (A.35),

$$\left(\frac{\partial \eta_{12}}{\partial x_j}\right)_2 = \frac{4}{\pi \omega n_1}\mathrm{Im}\left(\sum_{r,s} (\mathbf{E}\,\mathrm{Re}(\mathbf{C}))_{rs}\left(\frac{\partial \phi_2}{\partial x_j}\right)_{rs}\right). \tag{A.45}$$

Appendix A.4. Terms depending on the sensitivity of the direct field dynamic stiffness matrix of subsystem 1

The direct field dynamic stiffness matrix $\mathbf{D}'_{\mathrm{dir1}}$ is defined as

$$\mathbf{D}'_{\mathrm{dir1}} = \phi_1^{\mathrm{T}}\mathbf{D}_{\mathrm{dir1}}\phi_1 \tag{A.46}$$

with ϕ_1 the eigenvectors, used as a modal basis to describe the vibration field of the deterministic subsystem, of the part that is in contact with the first SEA subsystem; $\mathbf{D}_{\mathrm{dir1}}$ is the direct field dynamic stiffness matrix of the first SEA subsystem in terms of the physical coordinates of the deterministic subsystem.

Assuming that the design variables $\mathbf{x}$ are real values, the derivative of the imaginary part can be written as

$$\left(\frac{\partial \eta_{12}}{\partial x_j}\right)_3 := \frac{2}{\pi \omega n_1} \sum_{r,s} \mathbf{A}_{rs} \left(\mathbf{D}_{\text{tot}}^{-1} \frac{\partial}{\partial x_j} \left(\text{Im}\left(\mathbf{D}_{\text{dir1}}'\right)\right) \mathbf{D}_{\text{tot}}^{-H}\right)_{rs} \tag{A.47}$$

$$= \frac{2}{\pi \omega n_1} \sum_{r,s} \mathbf{A}_{rs} \left(\mathbf{D}_{\text{tot}}^{-1} \text{Im}\left(\frac{\partial \boldsymbol{\phi}_1^{\text{T}}}{\partial x_j} \mathbf{D}_{\text{dir1}} \boldsymbol{\phi}_1 + \boldsymbol{\phi}_1^{\text{T}} \mathbf{D}_{\text{dir1}} \frac{\partial \boldsymbol{\phi}_1}{\partial x_j}\right) \mathbf{D}_{\text{tot}}^{-H}\right)_{rs}. \tag{A.48}$$

This can be written as

$$\left(\frac{\partial \eta_{12}}{\partial x_j}\right)_3 = \frac{2}{\pi \omega n_1} \sum_{r,s} \mathbf{A}_{rs} \left(\mathbf{D}_{\text{tot}}^{-1} \text{Im}\left(\mathbf{J}^{\text{T}}\mathbf{G} + \mathbf{G}^{\text{T}}\mathbf{J}\right) \mathbf{D}_{\text{tot}}^{-H}\right)_{rs} \tag{A.49}$$

with

$$\mathbf{G} := \mathbf{D}_{\text{dir1}} \boldsymbol{\phi}_1 \text{ and } \mathbf{J} := \frac{\partial \boldsymbol{\phi}_1}{\partial x_j} \tag{A.50}$$

Using Property (A.9), the sensitivity becomes

$$\left(\frac{\partial \eta_{12}}{\partial x_j}\right)_3 = \frac{2}{\pi \omega n_1} \sum_{r,s} (\mathbf{A}(\mathbf{D}_{\text{tot}}^{-H})^{\text{T}})_{rs} \left(\mathbf{D}_{\text{tot}}^{-1} \text{Im}\left(\mathbf{J}^{\text{T}}\mathbf{G} + \mathbf{G}^{\text{T}}\mathbf{J}\right)\right)_{rs} \tag{A.51}$$

$$= \frac{2}{\pi \omega n_1} \sum_{r,s} (\mathbf{D}_{\text{tot}}^{-H}\mathbf{A}^{\text{T}})_{rs} \left(\text{Im}\left(\mathbf{J}^{\text{T}}\mathbf{G} + \mathbf{G}^{\text{T}}\mathbf{J}\right)^{\text{T}} (\mathbf{D}_{\text{tot}}^{-1})^{\text{T}}\right)_{rs} \tag{A.52}$$

$$= \frac{2}{\pi \omega n_1} \sum_{r,s} (\mathbf{D}_{\text{tot}}^{-H}\mathbf{A}^{\text{T}}\mathbf{D}_{\text{tot}}^{-1})_{rs} \left(\text{Im}\left(\mathbf{J}^{\text{T}}\mathbf{G} + \mathbf{G}^{\text{T}}\mathbf{J}\right)^{\text{T}}\right)_{rs} \tag{A.53}$$

$$= \frac{2}{\pi \omega n_1} \sum_{r,s} \mathbf{K}_{rs} \left(\text{Im}\left(\mathbf{J}^{\text{T}}\mathbf{G} + \mathbf{G}^{\text{T}}\mathbf{J}\right)\right)_{rs} \tag{A.54}$$

with

$$\mathbf{K} = \mathbf{D}_{\text{tot}}^{-H} \text{Im}\left(\mathbf{D}_{\text{dir2}}'\right) \mathbf{D}_{\text{tot}}^{-1} \tag{A.55}$$

The imaginary part of the matrix product can be written as the product of the imaginary and real parts as

$$\left(\frac{\partial \eta_{12}}{\partial x_j}\right)_3 = \frac{2}{\pi \omega n_1} \sum_{r,s} \mathbf{K}_{rs} \left(\text{Im}(\mathbf{J}^{\text{T}})\text{Re}(\mathbf{G}) + \text{Re}(\mathbf{J}^{\text{T}})\text{Im}(\mathbf{G}) + \text{Im}(\mathbf{G}^{\text{T}})\text{Re}(\mathbf{J}) + \text{Re}(\mathbf{G}^{\text{T}})\text{Im}(\mathbf{J})\right)_{rs} \tag{A.56}$$

Using Property (A.9), the sensitivity becomes

$$\left(\frac{\partial \eta_{12}}{\partial x_j}\right)_3 = \frac{2}{\pi \omega n_1} \sum_{r,s} (\mathbf{K}\,\text{Im}(\mathbf{G}^{\text{T}}))_{rs}\text{Re}(\mathbf{J}^{\text{T}}))_{rs} + (\mathbf{K}\,\text{Re}(\mathbf{G}^{\text{T}}))_{rs}\text{Im}(\mathbf{J}^{\text{T}}))_{rs} + \mathbf{K}_{rs}\left(\text{Im}(\mathbf{G}^{\text{T}})\text{Re}(\mathbf{J}) + \text{Re}(\mathbf{G}^{\text{T}})\text{Im}(\mathbf{J})\right)_{rs} \tag{A.57}$$

$$= \frac{2}{\pi \omega n_1} \sum_{r,s} (\mathbf{K}\,\text{Im}(\mathbf{G}^{\text{T}}))_{rs}\text{Re}(\mathbf{J}^{\text{T}}))_{rs}(\mathbf{K}\,\text{Re}(\mathbf{G}^{\text{T}}))_{rs}\text{Im}(\mathbf{J}^{\text{T}}))_{rs} + (\mathbf{K}^{\text{T}})_{rs}\left(\text{Im}(\mathbf{J}^{\text{T}})\text{Re}(\mathbf{G}) + \text{Re}(\mathbf{J}^{\text{T}})\text{Im}(\mathbf{G})\right)_{rs} \tag{A.58}$$

$$= \frac{2}{\pi \omega n_1} \sum_{r,s} (\text{Im}(\mathbf{G})\mathbf{K}^{\text{T}})_{rs}\text{Re}(\mathbf{J})_{rs} + (\text{Re}(\mathbf{G})\mathbf{K}^{\text{T}})_{rs}\text{Im}(\mathbf{J}))_{rs} + (\text{Im}(\mathbf{G})\mathbf{K})_{rs}\text{Re}(\mathbf{J})_{rs} + (\text{Re}(\mathbf{G}))_{rs}\text{Im}(\mathbf{J}))_{rs} \tag{A.59}$$

$$= \frac{4}{\pi \omega n_1} \text{Im}\left(\sum_{r,s}(\mathbf{G}\,\text{Re}(\mathbf{K}))_{rs}\,(\mathbf{J})_{rs}\right). \tag{A.60}$$

24

Or alternatively, with (A.50),

$$\left(\frac{\partial \eta_{12}}{\partial x_j}\right)_3 = \frac{4}{\pi\omega n_1}\text{Im}\left(\sum_{r,s}(\mathbf{G}\,\text{Re}(\mathbf{K}))_{rs}\left(\frac{\partial \phi_1}{\partial x_j}\right)_{rs}\right). \tag{A.61}$$

Appendix A.5. Synthesis

The following expression is found for the derivative by combining the terms (A.29), (A.45) and (A.61)

$$\frac{\partial \eta_{12}}{\partial x_j} = \frac{4}{\pi\omega n_1}\left[\text{Re}\left(\sum_{r,s}(-\mathbf{D}_{\text{tot}}^{-T}\mathbf{A}\mathbf{C}^{\text{T}})_{rs}\left(\frac{\partial \mathbf{D}_{\text{tot}}}{\partial x_j}\right)_{rs}\right) + \text{Im}\left(\sum_{r,s}(\mathbf{E}\,\text{Re}(\mathbf{C}))_{rs}\left(\frac{\partial \phi_2}{\partial x_j}\right)_{rs}\right) + \text{Im}\left(\sum_{r,s}(\mathbf{G}\,\text{Re}(\mathbf{K}))_{rs}\left(\frac{\partial \phi_1}{\partial x_j}\right)_{rs}\right)\right]. \tag{A.62}$$

The sensitivity of the total dynamic stiffness matrix can be further elaborated as

$$\frac{\partial \mathbf{D}_{\text{tot}}}{\partial x_j} = \frac{\partial \mathbf{D}_{\text{d}}}{\partial x_j} + \frac{\partial \mathbf{D}'_{\text{dir1}}}{\partial x_j} + \frac{\partial \mathbf{D}'_{\text{dir2}}}{\partial x_j} \tag{A.63}$$

$$= \frac{\partial \mathbf{D}_{\text{d}}}{\partial x_j} + \frac{\partial \phi_1^{\text{T}}}{\partial x_j}\mathbf{D}_{\text{dir1}}\phi_1 + \phi_1^{\text{T}}\mathbf{D}_{\text{dir1}}\frac{\partial \phi_1}{\partial x_j} + \frac{\partial \phi_2^{\text{T}}}{\partial x_j}\mathbf{D}_{\text{dir2}}\phi_2 + \phi_2^{\text{T}}\mathbf{D}_{\text{dir2}}\frac{\partial \phi_2}{\partial x_j} \tag{A.64}$$

References

[1] S. Marburg. Developments in structural-acoustic optimization for passive noise control. *Archives of Computational Methods in Engineering*, 9(4):291–370, 2002.

[2] H. Kim, S.Goo, J. Jung, and S. Wang. Design optimization of a cellular-type noise insulation panel to improve transmission loss at low frequency. *Journal of Sound and Vibration*, 447:105 – 119, 2019.

[3] M. Shimoda, K. Shimoide, and J. Shi. Structural–acoustic optimum design of shell structures in open/closed space based on a free-form optimization method. *Journal of Sound and Vibration*, 366:81 – 97, 2016.

[4] R. Picelli, W.M. Vicente, R. Pavanello, and Y.M. Xie. Evolutionary topology optimization for natural frequency maximization problems considering acoustic–structure interaction. *Finite Elements in Analysis and Design*, 106:56 – 64, 2015.

[5] D. Roca, D. Yago, J. Cante, O. Lloberas-Valls, and J. Oliver. Computational design of locally resonant acoustic metamaterials. *Computer Methods in Applied Mechanics and Engineering*, 345:161 – 182, 2019.

[6] M. Klaerner, M. Wuehrl, L. Kroll, and S. Marburg. Fea-based methods for optimising structure-borne sound radiation. *Mechanical Systems and Signal Processing*, 89:37 – 47, 2017. Modern Approach to Complex Dynamical Systems.

[7] J.C.E. Van den Wyngaert, M. Schevenels, and E.P.B. Reynders. Predicting the sound insulation of finite double-leaf walls with a flexible frame. *Applied Acoustics*, 141:93–105, 2018.

[8] P.J. Shorter and R.S. Langley. Vibro-acoustic analysis of complex systems. *Journal of Sound and Vibration*, 288(3):669–699, 2005.

[9] E. Reynders, R.S. Langley, A. Dijckmans, and G. Vermeir. A hybrid finite element - statistical energy analysis approach to robust sound transmission modelling. *Journal of Sound and Vibration*, 333(19):4621–4636, 2014.

[10] C. Decraene, A. Dijckmans, and E.P.B. Reynders. Fast mean and variance computation of the diffuse sound transmission through finite-sized thick and layered wall and floor systems. *Journal of Sound and Vibration*, 422:131–145, 2018.

[11] K.-U. Bletzinger, M. Firl, J. Linhard, and R. Wüchner. Optimal shapes of mechanically motivated surfaces. *Computer Methods in Applied Mechanics and Engineering*, 199:324–333, 2010.

[12] International Organization for Standardization. *ISO 717-1: Acoustics – Rating of sound insulation in buildings and of building elements – Part 1: Airborne sound insulation*, 1996.

[13] K.-U. Bletzinger, M. Firl, and F. Daoud. Approximation of derivatives in semi-analytical structural optimization. *Computers and Structures*, 86:1404–1416, 2008.

[14] H. Denli and J.Q. Sun. Structural-acoustic optimization of sandwich structures with cellular cores for minimum sound radiation. *Journal of Sound and Vibration*, 301(1):93–105, 2007.

[15] L. Meirovitch. *Elements of vibration analysis*. McGraw-Hill, New York, NY, 1975.

[16] P. Davidsson, J. Brunskog, P.-A. Wernberg, G. Sandberg, and P. Hammer. Analysis of sound transmission loss of double-leaf walls in the low-frequency range using the finite element method. *Building Acoustics*, 11(4):239–257, 2004.

[17] J. Brunskog and P. Davidsson. Sound transmission of structures. A finite element approach with simplified room description. *Acta Acustica united with Acustica*, 90(5):847–857, 2004.

[18] Y. Miki. Acoustical properties of porous materials - modifications of Delany-Bazley models. *Journal of the Acoustical Society of Japan*, 11(1):19–24, 1990.

[19] K.J. Bathe. *Finite Element Procedures*. Prentice-Hall, Englewood Cliffs, NJ, second edition, 1996.

[20] R.S. Langley and V. Cotoni. Response variance prediction for uncertain vibro-acoustic systems using a hybrid deterministic-statistical method. *Journal of the Acoustical Society of America*, 122(6):3445–3463, 2007.

[21] E.P.B. Reynders and R.S. Langley. Cross-frequency and band-averaged response variance prediction in the hybrid deterministic-statistical energy analysis method. *Journal of Sound and Vibration*, 428:119–146, 2018. Open access.

[22] E. Reynders, C. Van hoorickx, and A. Dijckmans. Sound transmission through finite rib-stiffened and orthotropic plates. *Acta Acustica united with Acustica*, 102(6):999–1010, 2016.

[23] M.J. Crocker and A.J. Price. Sound transmission using statistical energy analysis. *Journal of Sound and Vibration*, 9(3):469–486, 1969.

[24] R.S. Langley. Numerical evaluation of the acoustic radiation from planar structures with general baffle conditions using wavelets. *Journal of the Acoustical Society of America*, 121(2):766–777, 2007.

[25] D. J. Ewins. *Modal testing*. Research Studies Press, Baldock, U.K., second edition, 2000.

[26] E. Reynders. System identification methods for (operational) modal analysis: review and comparison. *Archives of Computational Methods in Engineering*, 19(1):51–124, 2012.

[27] International Organization for Standardization. *ISO 12999-1:2014: Acoustics – Determination and application of measurement uncertainties in building acoustics – Part 1: Sound insulation*, 2014.

[28] J. Haslinger and R.A.E. Mäkinen. *Introduction to shape optimization: Theory, Approximation and Computation*. SIAM, Philadelphia, USA, 1st edition, 2003.

[29] Halmos George T. *Roll forming handbook*. CRC Press, 2006.

[30] European Committee for Standardization. *EN 14353:2017: Metal beads and feature profiles for use with gypsum plasterboards - Definitions, requirements and test methods*, 2017.

[31] ASTM International. *ASTM C 754 – 18 : Standard Specification for Nonstructural Steel Framing Members*, 2018.

[32] D. Zwillinger. *CRC standard mathematical tables and formulae*. CRC press, 2002.